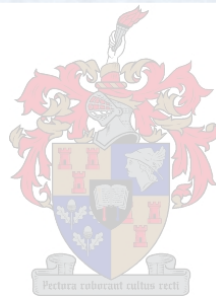


An Electro-Optic Measurement System for Electric Fields Near RF and Microwave Radiators and Scatterers

Jan Tait



Thesis presented in partial fulfillment of the requirements
for the degree of Master of Science in Engineering
at the University of Stellenbosch.

Supervisor: Prof. J. H. Cloete

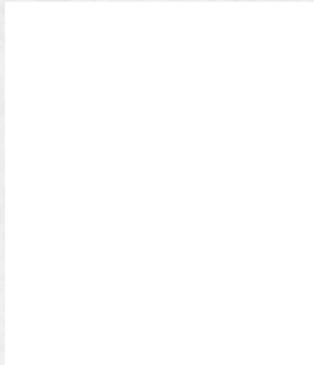
December 2000

Declaration

I, the undersigned, hereby declare that the work contained in this thesis is my own original work and that I have not previously in its entirety or in part submitted it at any university for a degree.

Signature:

Date:



Abstract

An electro-optic sensor system was developed which uses the modulated scatterer technique [1] to measure the fine structure—amplitude and phase—of electric fields with the minimum of perturbation. The theory for the technique is discussed in detail, with the Lorentz Reciprocity theorem as foundation. The system is also treated as a general two port and solved in terms of the impedances present. This comprises self impedances and mutual impedances.

The signals scattered by the dipole scatterer are modeled as amplitude modulated signals and a detailed detection scheme is presented. The detection of the signals is done by a digital correlation process. This is quite similar to synchronous detection.

A detailed sensitivity analysis is presented that was used to determine the quality of the system. This analysis is backed by a practical sensitivity measurement. A few antennas and scatterers are measured in the X-band using the system, and results are compared with theory. These systems include a pyramidal horn, an E-plane sectoral horn and a simple waveguide. Half plane diffraction by a metal sheet is also presented.

The practical implementation of the theory is emphasized.

Opsomming

'n Elektro-optiese meetsisteem is ontwikkel wat die gemoduleerde strooier tegniek [1] gebruik om die fyn struktuur—amplitude en fase—van elektriese velde te meet. Hierdie tegniek versteur die velde minimaal. 'n Volledige ondersoek word gedoen na die teorie van die stelsel. Die basis van die metode lê in die Lorentz Resiprook teorie. Alhoewel daar gekonsentreer word op hierdie teorie, is die stelsel ook beskou as 'n tweespoort. Die wedersydse en eie impedansies van die verskillende komponente word gebruik om die velde op te los.

Die gestrooide seine, as gevolg van die dipool strooier, word gemodelleer met behulp van amplitude modulاسie. Die deteksie van hierdie seine word deeglik bespreek. In plaas van 'n analoogstelsel, word 'n digitale korrelassie proses gebruik om die velde te meet.

Die sensitiwiteit van die stelsel word geanaliseer. Verder word metings met die stelsel geneem om die teoretiese analise te staaf. 'n Paar X-band sisteme word gebruik om metings te neem. Hierdie metings word ook vergelyk met teoretiese resultate. Stelsels wat gemeet is sluit die volgende in: 'n piramidale horing antenna, 'n E-vlak sektorale horing antenna, 'n X-band golfgeleier en die diffraksie op die rand van 'n plaat.

Die praktiese implementering van die teorie word beklemtoon.

Acknowledgements

I would like to acknowledge the following people for their contributions to this thesis.

Prof. J. H. Cloete for his guidance and enthusiasm.

Wessel Croucamp for the manufacturing of the needed equipment and antennas.

Jan Greyling for his assistance in the practical measurements.

My family, fiancé and friends for their support and prayers throughout the year.

My heavenly Father.

Keywords

Modulated Scatterer; Electric Field Measurement; Sensitivity; Reciprocity;
Uniform Theory of Diffraction

Abbreviations

RF Radio frequency

LO Local oscillator

IF Intermediate frequency

UTD Uniform theory of diffraction

GTD Geometrical theory of diffraction

IQ In-phase Quadrature-phase

AD Analog to digital

AM Amplitude modulation

DC Direct current

SNR Signal-to-noise ratio

ISB Incident shadow boundary

RSB Reflection shadows boundary

Contents

Declaration	I
Abstract	II
Opsomming	III
Acknowledgements	IV
Keywords	V
Abbreviations	VI
1 Introduction	1
2 The Modulated Scatterer Technique	3
2.1 Principle of Operation	3
2.2 Modulation of the Probe	4
2.2.1 Mechanical Modulation	4
2.2.2 Electrical Modulation	6
2.2.3 Light Modulation	6
2.2.4 Other Types of Probes	7
2.3 Modulation, Resonance and θ	7
2.4 Monostatic Method versus Bistatic Method	9
2.5 Multiple Probes and Arrays	10

CONTENTS

VIII

3	The Core of the Method	12
3.1	Lorentz Reciprocity	12
3.2	Determining the E-field Using Reciprocity	13
3.3	Impedance Matrix Formulation	14
3.4	Generalized Lorentz Reciprocity	16
3.5	Bistatic Scattering Formulation	18
3.6	Conclusion	21
4	Signals and Waves in the System	22
4.1	Amplitude Modulation	22
4.2	Noise	24
4.2.1	Noise Bandwidth	24
4.2.2	White Noise	25
4.2.3	Thermal Noise	25
4.2.4	Noise Figure	26
4.2.5	Noise Temperature	26
4.2.6	Noise in Cascaded Systems	27
4.2.7	Antenna Noise Temperature	27
4.2.8	Quantization Noise	27
4.3	Signal-to-Noise Ratio	29
4.3.1	Signal-to-Noise Ratio in Amplitude Modulation	29
4.3.2	Improving the Signal-to-Noise Ratio	30
4.4	Correlation	30
4.4.1	The Mathematical Model of Correlation	31
4.4.2	Correlation used in the Modulated Scatterer System	31
4.5	Detailed Detection Scheme	32
4.6	Mechanical Modulation	35
5	Sensitivity Analysis	37
5.1	Analysis of the System Sensitivity	38

CONTENTS

IX

5.2	Measurement of the Linearity	39
5.3	Calculations on Sensitivity Measurements	40
6	Practical Implementation	44
6.1	The Probe	44
6.2	IQ-Detector	45
6.3	Description of the Measurement Setup	45
6.4	Computation of the Field from the Measured Data	48
7	Practical Measurements	49
7.1	Pyramidal Horn	49
7.2	E-Plane Sectoral Horn	54
7.3	A Simple Waveguide	56
7.4	Diffraction by a Half Plane	58
8	Conclusion	63
A	Component Listing	65
B	Photos	66
C	Uniform Theory of Diffraction	69
C.1	Elementary Theory	69
C.2	Equations of the UTD	72
D	Theory of the E-plane Sectoral Horn	75
D.1	Computing the Fundamental Wave	75
D.2	Hankel Functions	78
D.3	Computing the Diffraction Fields	79
D.3.1	First Order Diffraction Fields	81
D.3.2	Second Order Diffraction Fields	82

<i>CONTENTS</i>	X
E Design of the E-Plane Sectoral Horn	83
F MATLAB Program Code	84
F.1 Computation of the E-field from the Measured Data	84
F.2 Hankel Functions	86
F.2.1 Hankel Function	86
F.2.2 Derivative of the Hankel Function	86
F.3 Diffraction Coefficient Computation	87
F.3.1 Fresnel Integral Computation	87
F.3.2 Computation of the Diffraction Coefficients	88
F.4 E-Plane Horn Antenna Field Calculation	89
G FEKO Program Code	94
G.1 Marconi Pyramidal Horn	94
G.2 E-Plane Sectoral Horn	96
H Datasheet of the OP500 Phototransistor	99

List of Figures

2.1	Mechanical modulation.	5
2.2	Placing the modulated scatterer in the E-field.	6
2.3	The basic monostatic measurement setup.	8
2.4	The basic bistatic measurement setup.	9
2.5	The use of multiple probes.	10
2.6	Three-axis probe.	10
3.1	Region for the analysis of the Lorentz reciprocity theorem. . .	13
3.2	Four-terminal network representation.	14
3.3	The reciprocity theorem.	18
3.4	Three-port diagram of the bistatic measurement setup.	19
4.1	Voltage and frequency spectrum for AM-modulation.	23
4.2	The components of vector V_s	34
4.3	Mechanically modulated probe in an elliptical E-field.	35
5.1	Detailed configuration used for the sensitivity analysis.	37
5.2	Measurement of the system linearity.	41
5.3	Error in the linearity measurement.	41
5.4	X-band waveguide.	42
6.1	Construction of the probe.	44
6.2	IQ-detector construction.	45
6.3	Detailed configuration used for the measurements.	46

LIST OF FIGURES

XII

6.4	Structure used in the measurements.	47
7.1	Geometry of the pyramidal horn antenna measured.	49
7.2	Marconi pyramidal horn field - amplitude.	50
7.3	Marconi pyramidal horn field - phase.	50
7.4	Full Marconi pyramidal horn field - amplitude.	51
7.5	Full Marconi pyramidal horn field - phase zoomed.	52
7.6	Full Marconi pyramidal horn field - phase.	52
7.7	Marconi pyramidal horn field - amplitude, horn rotated.	53
7.8	Marconi pyramidal horn field - phase, horn rotated.	53
7.9	E-plane sectoral horn.	54
7.10	E-plane sectoral horn field - amplitude.	55
7.11	E-plane sectoral horn field - phase.	55
7.12	A simple waveguide.	56
7.13	Waveguide field measurement - amplitude.	57
7.14	Waveguide field measurement - phase.	57
7.15	Diffraction measurement - amplitude.	58
7.16	Diffraction measurement - phase.	59
7.17	Diffraction measurement - amplitude.	59
7.18	Diffraction measurement - phase.	60
7.19	Half plane diffraction: GO field.	61
7.20	Half plane diffraction: total electric field.	61
7.21	Half plane diffraction: diffraction fields.	61
B.1	Pyramidal horn antenna with probe.	66
B.2	The E-plane horn and probe.	66
B.3	Busy with a setup.	67
B.4	The complete setup.	67
B.5	Electronics as seen from the top.	68
B.6	IQ-detector	68

LIST OF FIGURES

XIII

C.1	Different planes and boundaries of a wedge.	70
C.2	Diffraction in a non-principle plane.	71
C.3	Diffraction in the non-principle plane – top view.	71
D.1	Wedged plate configuration.	76
D.2	Diffraction along the y-axis of the E-plane horn antenna.	79
D.3	Geometry of the E-plane horn antenna fields.	80
D.4	Determining the angle φ_1	82
E.1	Geometry of the designed E-plane horn.	83

List of Tables

5.1	Component specifications	38
5.2	Measurement of the linearity: an example	40
A.1	List of Components	65

Chapter 1

Introduction

Measurements of electric and magnetic fields inevitably cause perturbations of the field distributions. The conventional method of measurement—with antenna probes and connecting conductors and waveguides, typically several wavelengths in size—causes considerable damage to the measured field pattern. This prevents the accurate measurement of fields, especially close to the source antenna. Reasons are as follows, [1]:

1. Standing waves are set up between the probe antenna and any nearby conducting object. This includes the source antenna. The result is a distortion of the measured fields.
2. The field pattern varies rapidly with position close to a conductor (in general), because of the presence of evanescent waves and interference between travelling waves. Conventional probes suffer lack of resolution, because of their physical size.
3. Antennas radiate in various directions. Because the gain of conventional probes vary with direction, it causes a measurement uncertainty which is a function of the angle of incidence.

An improved system should overcome these restrictions and disadvantages. Properties of the new system should include most of the following [2]:

- The method must be able to measure the fine structure in the electric field
- The method must be able to measure amplitude and phase

- Field perturbation should be minimal
- The probe must be able to distinguish between different components of the field
- The sensitivity of the system should be such that a good dynamic range can be obtained
- Measurements should be simple and inexpensive

The optically modulated scatterer is a passive device, which responds directly to the E-field. Although very small, with no electrical connections, it emits a scattered wave proportional to the square of the electric field incident on it. The physical size of the dipole probe is such that perturbation is at a minimum. For this reason, the optically modulated scatterer can be used where conventional probes would cause too much distortion [3]. The resolution is equal to the physical size, which is much less than conventional probes. The method can also be used to measure fields within a fraction of a wavelength from a conductor [4].

The amplitude and phase of the scattered wave are measured at the receiver antenna, and the amplitude and phase of the electric field—at the position of the scatterer—are calculated. To recognize the very small scattered signal from other unwanted signals (like fields scattered from edges of the source antenna), the scatterer is modulated at its centre with a photodiode or phototransistor at a low frequency (typically in the audio range in the order of 1 kHz to 10 kHz). Instead of using electrical conductors to modulate the dipole (for example with a normal diode or resistive element), optic fiber is used to guide a modulated laser beam to the photo device. No electrical connections are made, limiting perturbation to a minimum.

Chapter 2

The Modulated Scatterer Technique

An overview of the modulated scatterer technique is given. The different modulation techniques are discussed with their advantages and disadvantages. The difference between the monostatic and bistatic setup is highlighted and the possibility of multiple probes and multidimensional probes are considered.

2.1 Principle of Operation

When placing an antenna in an electric field, a voltage and current is generated at the antenna terminals. When the antenna is not perfectly matched to its surrounding environment, the antenna reflects some of the energy that is incident upon it. The field incident upon an antenna will also scatter from its conducting wires and edges.

If the RF-impedance of an antenna can be varied, the amount of energy that is reflected can be varied. It is however not necessary to know the exact impedance of the antenna used. If there is a change in the impedance, there will be a change in the scattered field. The change in the scattered field can be measured to give an indication of the field at the antenna, because the percentage of the field scattered will not vary with the field strength at the antenna, but will only be a function of the depth of modulation of the RF-impedance of the scatterer antenna.

The modulated scatterer utilizes this principle. A small dipole, with size only

a fraction of the wavelength of the frequency to be measured (dimension usually shorter than half a wavelength [5]), is used as the antenna which acts as a scatterer. The scattered signal is then an indication only of the amplitude and phase of the electric field at the position of the probe. It is not a function of the position itself [1, 4]. In chapter 3 it will be shown by use of the reciprocity principle, that the received scattered signal is independent of the paths of the scattered signal. This holds true for the monostatic method, but is more complex when the bistatic method is used (section 2.4).

The scatterer need not be modulated to receive a backscattered signal from it. However, due to a multitude of reflections from other sources, there must be a way to distinguish between these unwanted scatterings and reflections, and the scattering from the measurement probe. By modulating the probe, the change in the scattered field will thus represent the field at the position of the probe.

Instead of using a modulation technique to retrieve the electric field data, it is possible to use a time-gating or time-separation technique to determine the magnitude and phase of the field at the scatterer's position [6]. However, this could become a very complicated process, and it was not further investigated.

2.2 Modulation of the Probe

To vary the percentage of the field scattered by the modulated scatterer probe, the RF-impedance of the probe should be changed. There are several ways of accomplishing this, and it is worth the while to look at the different techniques.

2.2.1 Mechanical Modulation

Probably the most effective way (but not necessarily the best or easiest method) of modulating the probe, is via mechanical vibration or spinning. By spinning the dipole in a plane, with the spin-axis normal to the E-field component, modulation of the incident E-field on the probe, parallel to the length of the probe, can be obtained [7, 8]. It is also possible to change the self-impedance of the dipole by stretching and compressing it, thus changing the length of the dipole [2].

Figure 2.1 shows the E-field incident at an angle $\theta_E = 90^\circ$ on the probe. The probe is spun at an angular rate of Ω radians per second in the yz-plane. The

E-field is y-directed. As will be shown in section 4.6, the modulation of the backscattered wave will be at a frequency of 2Ω radians per second—twice the angular frequency of the motor—after filtering.

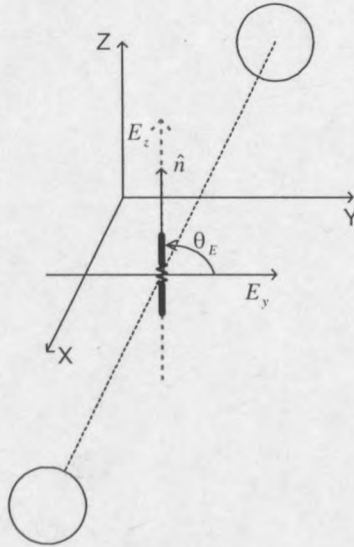


Figure 2.1: Mechanical modulation: spinning the probe in the E-field.

This method does have drawbacks, however. Firstly, it is not possible to measure, for example, inside cavities or aperture antennas, because of the strings attached to the probe. Mechanical modulation is thus constrained to unobstructed areas only. This limits the use of the method. Secondly, it is very difficult to distinguish between the different components of the E-fields, as will be explained in section 4.6. In figure 2.1, an extra z-directed E-field as shown would cause a strong reflection when $\theta = 90^\circ$ with respect to E_y . There are other drawbacks as well, like the effect of mechanical ringing, which should be allowed to stabilize before measurements commence. Also, the mechanical process limits the modulating frequency to the lower hundreds of Hertz, thereby restricting the detection system's sensitivity (because of the $\frac{1}{f}$ -noise).

Despite these negative factors, there are a few positive ones that should be kept in mind. For one, the depth of modulation is superior to that obtained using a photosensitive probe. If the scatterer is made resonant (which is much easier in the case of a plain dipole), the backscattered signal can be enhanced, allowing even smaller E-fields to be detected. The size of the probe is not limited by a phototransistor, diode or other type of photocell. This allows very high frequencies to be measured.

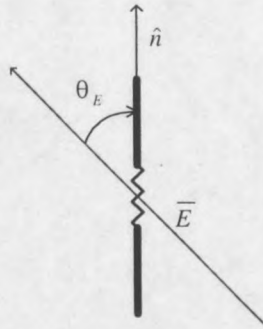


Figure 2.2: Placing the modulated scatterer in the E-field.

2.2.2 Electrical Modulation

By placing the dipole scatterer with its axis (\hat{n}) parallel to the E-field component to be measured, as shown in figure 2.2 when $\theta_E = 0^\circ$, the scattered signal will represent the specific component of the E-field.

To modulate the scattered field, a nonlinear impedance, like a diode, is placed at the dipole's centre. By applying an audio voltage through slightly conducting leads, the impedance of the dipole can be switched, thereby varying the scattered signal [8]. A few remarks would be in order. The conductive leads should have a very high resistance, as well as a small diameter, as not to disturb the measured fields too much. If possible, the conductive leads should be placed orthogonal to the E-field vector.

Other than in the case of the mechanical modulated scatterer, placement of the probe is much easier. Because the field parallel to the probe is the component scattered (and modulated), it is also possible to easily single out different components of the fields. This enhances the measurement technique.

2.2.3 Light Modulation

Replacing the device at the centre of the dipole with a photosensitive device, like a photodiode or phototransistor, eliminates the need for conductive leads. By modulating the photo device with a light signal, the RF-impedance of the dipole can be switched at an audio frequency.

With the photo device as the modulating element, it is very important to look at the depth of modulation. If the photo-emitter and photoreceiver are matched, the depth of modulation will be very good. If it is not matched, the

modulation depth will be less, which leads to inferior results. According to [5], the type of probe used is significant. Using a better probe will enhance the dynamic range of the system. For example, [5] used a phototransistor probe with a dynamic range in the order of 23 dB, but this was improved by using a probe with a gallium arsenide switch to a dynamic range greater than 60 dB.

The use of phototransistors and photodiodes is a very attractive option, because not only is the probe very easy to implement, but the components are readily available. By using these probes, and carefully setting up the measurement equipment and light modulation setup, it is possible to achieve a dynamic range which exceeds 60 dB.

2.2.4 Other Types of Probes

It is possible to use photocells at the centre of the probe. By illuminating the photocell, its resistance changes, thereby changing the impedance of the probe [9].

Furthermore, it is possible to use a phosphoric element to heat a thermometer, which is situated at the probe's centre. The phosphoric element is heated via a light signal—modulated at an audio frequency—and this heats the thermometer. The heated thermometer has a different impedance, changing the impedance of the dipole probe [10].

The use of active scatterers has also been reported [11]. It was proposed here to use tunnel diodes to provide a negative resistance load to the centre of the dipole. The negative resistance enhances the scattered signal. This creates the possibility of using very small scatterers—thus eliminating perturbation—while enhancing the scattered signal and thus sensitivity and dynamic range.

2.3 Modulation, Resonance and θ

The scattered field is found to be amplitude modulated. The frequency of the carrier wave is equal to the frequency of the microwave or RF source, while the modulating frequency is equal to the modulating frequency of the impedance at the dipole centre. As will be shown in section 4.1, the modulation has the typical characteristics of large carrier amplitude modulation. Other types of modulation can be obtained, but this involves the use of RF circuitry at the

scatterer, making it larger and thus less attractive, because of an increase in field perturbation.

The scatterer can be resonant or non-resonant. If the scatterer is made resonant, it will enhance the scattered signal. This will enable measurement at greater distances and of smaller signals. Because a resonant scatterer enhances the modulation effect, the depth of modulation will be increased. This will enhance the dynamic range.

The alignment of the probe with respect to the electric field is also very important. According to figure 2.2, the electric field parallel to the dipole will be $E = |\mathbf{E}| \cos(\theta_E)$. Therefore, the greater the angle between the probe and the electric field vector, the smaller the reflection. An angle of $\theta = 90^\circ$, will result in the incident field on the scatterer being zero. There will thus be no field scattered, and the field measured will be zero. This is an obvious advantage, as it creates the possibility to measure the different polarization components of an electric field.

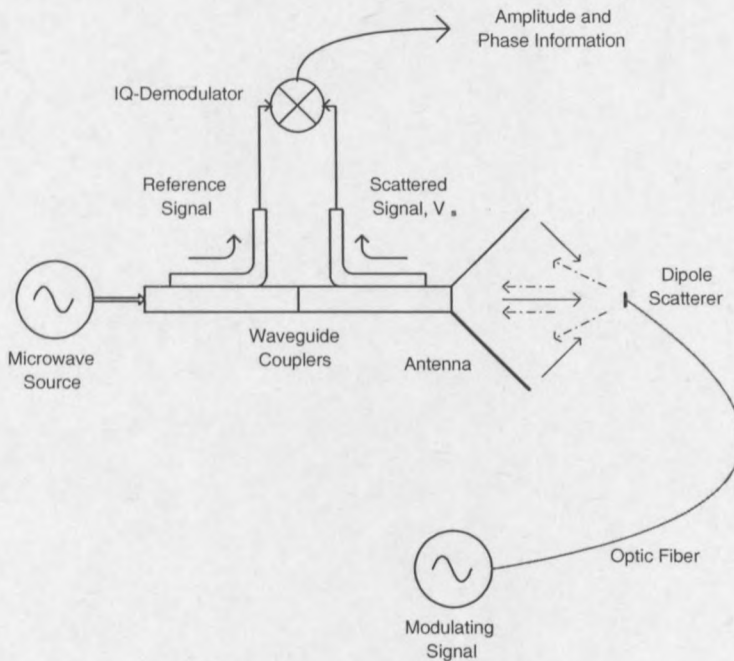


Figure 2.3: The basic monostatic measurement setup: the source antenna is used as the detector antenna.

2.4 Monostatic Method versus Bistatic Method

The electric field incident on the modulated scatterer probe is scattered in all directions. When the monostatic method is used, the transmitting antenna also acts as the receiving antenna, as can be seen in figure 2.3.

In this reciprocal system, the received signal is proportional to the square of the electric field incident on the modulated dipole probe. As will be shown in chapter 3, the scattered signal received at the source antenna is a function only of the electric field incident on the scatterer at the position of the scatterer. It is totally independent of the path lengths and attenuation to and from the scatterer.

In the bistatic system, however, the receiving antenna is separate from the transmitting antenna, as can be seen in figure 2.4.

The signal received in the receiver antenna is more complex than in the case of the monostatic method. The reciprocity theory—as used for the monostatic method—cannot be used here. A derivation for a three-port system should

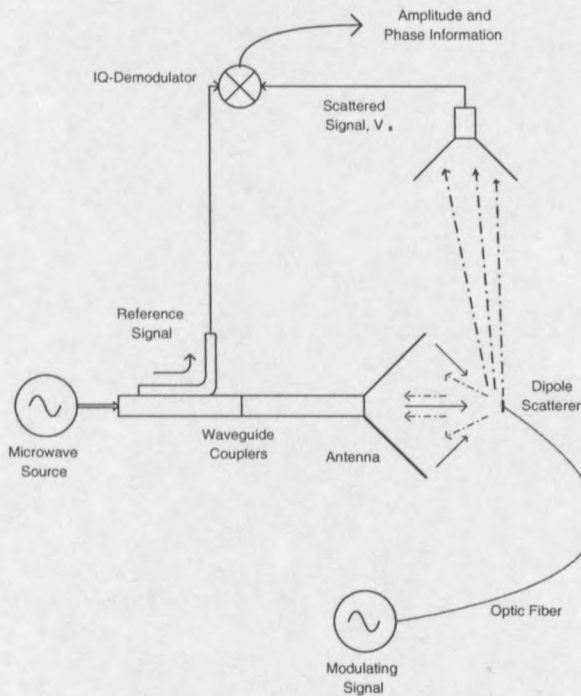


Figure 2.4: The basic bistatic measurement setup: an independent antenna is used as the detector antenna.

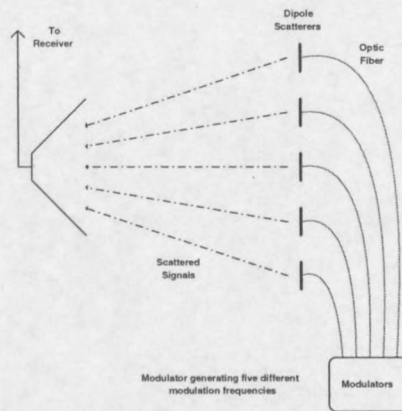


Figure 2.5: The use of multiple probes.

be done instead.

2.5 Multiple Probes and Arrays

It is possible to use more than one scatterer at the same time (see figure 2.5). By modulating each scatterer at a different modulating frequency, the field at each probe can be obtained simultaneously. It is, however, important to note that if the scatterers are positioned too close to each other, they will couple with each other, and the measurement will not be accurate if it is not compensated for. The fields that are measured will be disturbed more than in the case of the single scatterer. This may cause the method to lose its validity.

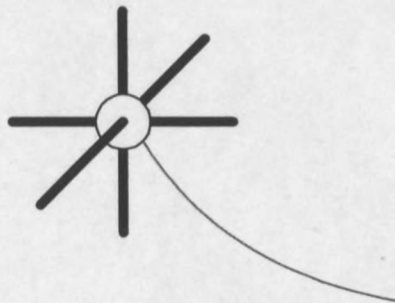


Figure 2.6: Three-axis probe.

CHAPTER 2. THE MODULATED SCATTERER TECHNIQUE 11

In a cartesian coordinate system, all three components of the field (E_x , E_y and E_z) can be measured almost simultaneously by constructing a probe as shown in figure 2.6. The probe has a dipole on all three axes. The dipoles are modulated in turn and the field components are measured accordingly [12]. The orthogonal components do not have any effect on the respective dipoles, as was explained in section 2.3. Because of the small finite diameter of the probes, the effect of the scatterings of the electric fields normal to the probe will be negligible.

Chapter 3

The Core of the Method

The basis of the theory of the modulated scatterer is the Lorentz reciprocity theorem. This theorem can be found in almost any textbook covering electromagnetic theory [13, 14, 15, 16]. Another good reference is [7].

3.1 Lorentz Reciprocity

The Lorentz reciprocity theorem can be derived from Maxwell's equations and is written as [14, 15]

$$-\nabla \cdot (\mathbf{E}_1 \times \mathbf{H}_2 - \mathbf{E}_2 \times \mathbf{H}_1) = \mathbf{E}_1 \cdot \mathbf{J}_2 + \mathbf{H}_2 \cdot \mathbf{M}_1 - \mathbf{E}_2 \cdot \mathbf{J}_1 - \mathbf{H}_1 \cdot \mathbf{M}_2 \quad (3.1)$$

in differential form and as

$$-\oint_S (\mathbf{E}_1 \times \mathbf{H}_2 - \mathbf{E}_2 \times \mathbf{H}_1) \cdot d\mathbf{s} = \iiint_V (\mathbf{E}_1 \cdot \mathbf{J}_2 + \mathbf{H}_2 \cdot \mathbf{M}_1 - \mathbf{E}_2 \cdot \mathbf{J}_1 - \mathbf{H}_1 \cdot \mathbf{M}_2) dv \quad (3.2)$$

in integral form. If the region under consideration is source-free ($\mathbf{J}_1 = \mathbf{J}_2 = \mathbf{M}_1 = \mathbf{M}_2 = 0$), the right-hand sides of the above equations vanish, and they become

$$\begin{aligned} -\nabla \cdot (\mathbf{E}_1 \times \mathbf{H}_2 - \mathbf{E}_2 \times \mathbf{H}_1) &= 0 \\ -\oint_S (\mathbf{E}_1 \times \mathbf{H}_2 - \mathbf{E}_2 \times \mathbf{H}_1) \cdot d\mathbf{s} &= 0 \end{aligned} \quad (3.3)$$

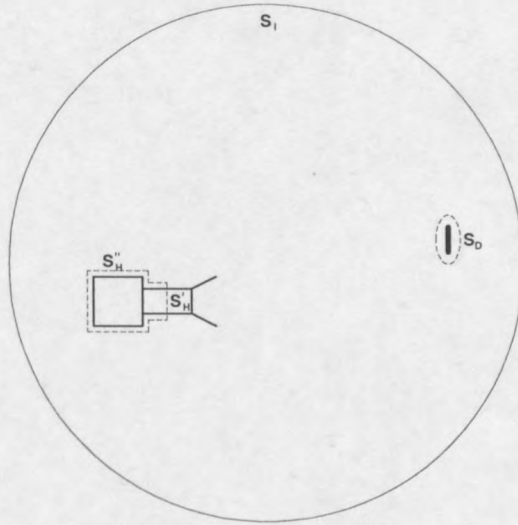


Figure 3.1: Region for the analysis of the Lorentz reciprocity theorem.

3.2 Determining the E-field Using Reciprocity

In figure 3.1, S_I is the surface of an infinitely large sphere including the measurement apparatus. S_H is the surface containing the microwave source and the transmitting antenna. S_D contains the small dipole scatterer. Clearly, equation 3.3 can be written as

$$\oint_S (\mathbf{E}_1 \times \mathbf{H}_2) \cdot d\mathbf{s} = \oint_S (\mathbf{E}_2 \times \mathbf{H}_1) \cdot d\mathbf{s} \quad (3.4)$$

This equation will hold between any two fields satisfying Maxwell's equations everywhere in the volume S_I , excluding the sources. \mathbf{E}_1 and \mathbf{H}_1 are the fields produced by the microwave source and antenna. \mathbf{E}_2 and \mathbf{H}_2 are the fields produced by the dipole scatterer, with dipole moment \mathbf{P} . The system is assumed to be matched, and therefore no reflections will cause interference as a result of unwanted waves.

The integral in equation 3.4 is broken up according to the different surfaces, so that the integral becomes

$$\oint_{S_I} (\mathbf{E}_1 \times \mathbf{H}_2) \cdot d\mathbf{s} + \oint_{S_H} \dots + \oint_{S_D} \dots = \oint_{S_I} (\mathbf{E}_2 \times \mathbf{H}_1) \cdot d\mathbf{s} + \oint_{S_H} \dots + \oint_{S_D} \dots \quad (3.5)$$

It can be shown that this integral equation is satisfied everywhere in the

system and on the surfaces [7]. By taking the magnitudes of the fields in the source antenna (at S_H) as respectively α for \mathbf{E}_1 and β for \mathbf{E}_2 and given that \mathbf{E}_1 has a distribution function of $\mathbf{F}(x, y, z)$, it can be proven from equation 3.5 that [7]

$$\beta = \alpha k (\boldsymbol{\eta} \cdot \mathbf{F})^2 \quad (3.6)$$

with

$$k = \frac{j\omega\zeta Z_0}{ab} \quad (3.7)$$

\mathbf{F} takes the value at the position of the scatterer, and k is a constant determined by the frequency (ω), the dimensions of the X-band waveguide feed (a and b) and the polarizability (ζ) of the dipole scatterer. $\boldsymbol{\eta}$ is the vector parallel to the dipole scatterer. Z_0 is the impedance in the waveguide, and is given by $Z_0 = \sqrt{\frac{\mu_0}{\epsilon_0} \frac{\lambda_g}{\lambda}}$.

3.3 Impedance Matrix Formulation

It is possible to model the system as a conventional four-terminal network, as can be seen in figure 3.2 [2].



Figure 3.2: Four-terminal network representation of the source and scatterer [17].

The network has the impedance matrix $[Z]$, so that $[V] = [Z][I]$, or

$$V_1 = Z_{11}I_1 + Z_{12}I_2$$

$$V_2 = Z_{21}I_1 + Z_{22}I_2 \quad (3.8)$$

By taking Z_L as the impedance at the centre of the dipole scatterer, the voltage at the dipole terminals will be $V_2 = -I_2Z_L$. The voltage, V_1 , can now be written in terms of the impedances and the current, I_1 , as

$$V_1 = \left[Z_{11} - \frac{Z_{12}Z_{21}}{Z_{22} + Z_L} \right] I_1 \quad (3.9)$$

Without the scatterer present, I_2 and V_2 will be zero. Therefore, with V'_1 representing the voltage without the scatterer present, and Z'_{11} representing the input impedance at the source antenna without the scatterer present

$$V'_1 = I_1Z'_{11} \quad (3.10)$$

The voltage will be modulated. Subtracting the voltage in the absence of the scatterer from the voltage when the scatterer is present, will give the signal in the presence of the modulating scatterer [18]

$$V_1 - V'_1 = \Delta V_1 = \left[(Z_{11} - Z'_{11}) - \frac{Z_{12}Z_{21}}{Z_{22} + Z_L} \right] I_1 \quad (3.11)$$

Assuming the medium is linear and reciprocal (see section 3.1), the impedance matrix will be symmetric, and $Z_{12} = Z_{21}$. Z_L is purposely modulated. This modulation of Z_L has an effect on the self-impedance of the source antenna, $Z_{11} = \frac{V_1}{I_1} |_{I_2=0}$, where V_1 is the voltage at the source antenna. $(Z_{11} - Z'_{11})$ represents the change in the input impedance of the transmit-receive antenna, due to the scatterer. This impedance change with the position and orientation of the scatterer, but is evidently very small. The term is lost in the detection process and can thus be ignored [18].

$Z_{22} = \frac{V_2}{I_2} |_{I_1=0}$, the self-impedance of the scatterer, will also change with the position and orientation of the scatterer. This will in effect contribute to a small measurement error.

The impedance matrix elements can be computed in terms of the fields as [17, 2, 18]

$$Z_{ij} = \frac{-1}{I_i I_j} \int_{\tau_i} \mathbf{E}_j \cdot \mathbf{J}_i d\tau = \frac{V_{ij}}{I_j} \quad (3.12)$$

I_i and I_j are the input currents at the respective terminal with the other terminal open-circuited. V_{ij} is the voltage at terminal i due to the current

source at terminal j . τ_i is the volume of antenna i , driven by I_i . Equation 3.12 is a consequence of the reciprocity theorem (section 3.1).

From equation 3.12,

$$Z_{21} = \frac{-1}{I_1 I_2} \int_{\tau_2} \mathbf{E}_1 \cdot \mathbf{J}_2 d\tau = Z_{12} \quad (3.13)$$

\mathbf{E}_1 is the E-field at the position of the scatterer—should the scatterer be absent—when the microwave source is driven by a current I_1 . \mathbf{E}_1 is taken as uniform over the length of the dipole. Therefore

$$Z_{21} \cong \frac{-\mathbf{E}_1 \cdot \boldsymbol{\eta} l_e}{I_1} \quad (3.14)$$

with $\boldsymbol{\eta}$ the vector parallel to the dipole. l_e is the effective length of the dipole, given as [18]

$$l_e = \frac{1}{I_2(0)} \int_{l_{dipole}} I_2(l) dl \quad (3.15)$$

with $I_2(0)$ the current at the centre of the dipole.

Substituting equation 3.14 into equation 3.11, and realizing that $E_1 = \mathbf{E}_1 \cdot \boldsymbol{\eta}$, gives for ΔV_1

$$\Delta V_1 = (Z_{11} - Z'_{11}) I_1 - \frac{(E_1 l_e)^2}{I_1 (Z_{22} + Z_L)} \quad (3.16)$$

Therefore, ignoring the effect of $(Z_{11} - Z'_{11})$ —which mostly accompanies mechanical modulation [2]—it can be seen that the voltage detected is proportional to the square of the electric field incident on the modulated scatterer probe.

3.4 Generalized Lorentz Reciprocity

A special case of the reciprocity principle is taken as a starting point [1]. Here it is important to realize that a monostatic method is used, which simplifies the theory.

It will be proved that the voltage measured at the detector, due to the scatterer, is a function of the electric field at the scatterer, which can be expressed as

$$V_s = kE^2 \quad (3.17)$$

In this equation, V_s is the complex voltage measured at the output of the detector, E is the complex electric field parallel to the dipole scatterer, and k is a constant characteristic of the probe. The probe should be calibrated to determine this constant.

Take the scatterer as a short, straight, thin wire (dipole) of length 2δ parallel to vector $\boldsymbol{\eta}$. \boldsymbol{E} , a complex vector, represents the electric field at the position of the scatterer, if it were absent. An electric dipole (with a separation of 2δ between the charges) has a dipole moment of amplitude $P = 2\delta q$, with a direction from the negative to the positive charge [16]. The oscillating electric field thus sets up an oscillating dipole moment, \boldsymbol{P}_s , which is also complex. \boldsymbol{P}_s is parallel to $\boldsymbol{\eta}$ and, if the scatterer is small ($\delta \ll \lambda$), proportional to \boldsymbol{E} . This gives the following equation

$$\boldsymbol{P}_s = \beta(\boldsymbol{\eta} \cdot \boldsymbol{E})\boldsymbol{\eta} \quad (3.18)$$

By modulating the photodiode in the centre of the dipole, β is varied, for β is determined by the input impedance of the dipole. Varying β , modulates the scattered wave.

Because of the finite size of the dipole, the response of the scatterer is an average over the length of the dipole, and not the value $\boldsymbol{\eta} \cdot \boldsymbol{E}$ at the centre. Equation 3.18 is thus an approximation.

The backward wave in the source antenna (the scattered wave) undergoes attenuation and a phase change, as it is traveling from the scatterer towards the point where it is measured at the antenna. It is easy to see that the relation of this wave to the dipole moment of the scatterer, \boldsymbol{P}_s , is a complex function of position of the scatterer. The forward wave (emitted from the source) undergoes this same attenuation and phase change from the measurement point to the scatterer. According to the reciprocity principle [1]

$$\boldsymbol{E}_s \cdot \boldsymbol{P} = \boldsymbol{E} \cdot \boldsymbol{P}_s \quad (3.19)$$

Although the microwave source is not a dipole, it can equivalently be replaced by a dipole. Evidently, the complex measured potential, V_s , is proportional



Figure 3.3: The reciprocity theorem [1].

to the left-hand side of equation 3.19. \mathbf{P} does not change as the scatterer is moved around (because the source antenna is stationary) and \mathbf{E}_s is in the same mode as \mathbf{E} at the source antenna (because of reciprocity). Equation 3.19 thus becomes

$$V_s = \alpha \mathbf{E} \cdot \mathbf{P}_s \quad (3.20)$$

Substituting for \mathbf{P}_s from equation 3.18, equation 3.20 becomes

$$V_s = \alpha \beta (\boldsymbol{\eta} \cdot \mathbf{E})^2 \quad (3.21)$$

Setting $k = \alpha \beta$ and with $E = (\boldsymbol{\eta} \cdot \mathbf{E})$, equation 3.17 is obtained. By modulating β , a modulation in k is obtained. This in turn causes a modulation of the complex voltage, V_s , such that equation 3.17 becomes

$$\Delta V = \Delta k E^2 \quad (3.22)$$

Due to the low frequency modulation, ΔV is easily measured amongst other scattered signals. This is done by IQ-detection.

3.5 Bistatic Scattering Formulation

Figure 2.4 shows the bistatic measurement system. This system can be seen as a linear three-port system such as the one displayed in figure 3.4.

This system has the matrix representation

$$\begin{bmatrix} V_1 \\ V_2 \\ V_3 \end{bmatrix} = \begin{bmatrix} Z_{11} & Z_{12} & Z_{13} \\ Z_{21} & Z_{22} & Z_{23} \\ Z_{31} & Z_{32} & Z_{33} \end{bmatrix} \begin{bmatrix} I_1 \\ I_2 \\ I_3 \end{bmatrix} \quad (3.23)$$

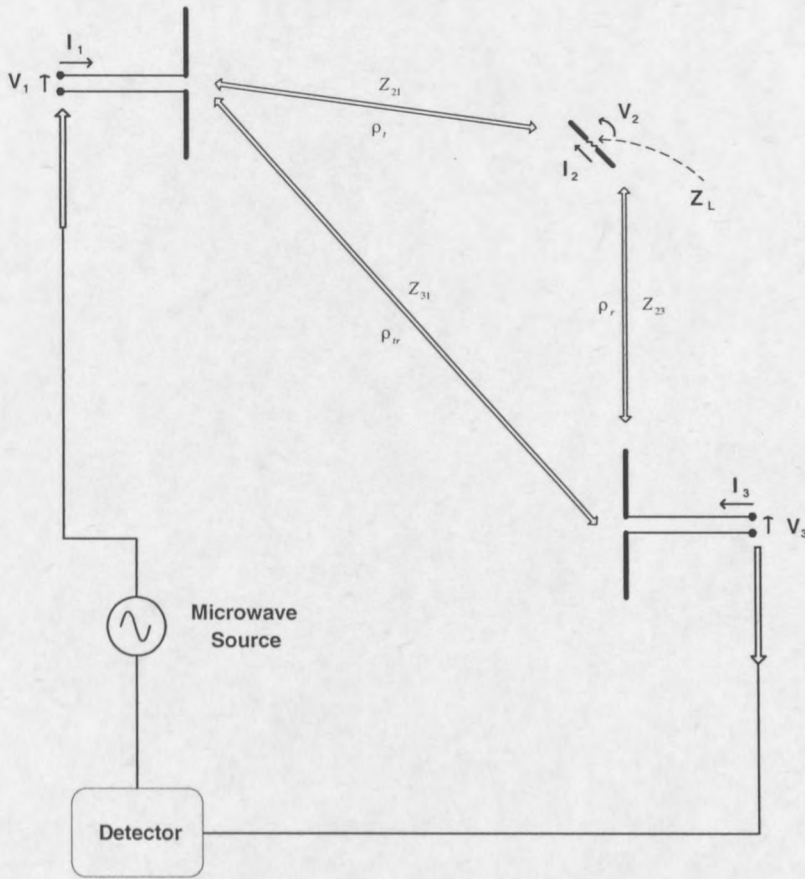


Figure 3.4: Three-port diagram of the bistatic measurement setup.

The desired signal to be found would be V_3 , the signal in the receiver antenna, and not V_1 as in the case for the monostatic measurement system. By specifying that V_3 is the open-circuit voltage, the current, I_3 , would be zero. The actual voltage at the receiving antenna terminals is in direct proportion to the open circuit voltage. The assumption that V_3 is the open-circuit voltage is therefore sufficient [2]. Setting I_3 equal to zero results in the third column of the impedance matrix in equation 3.23, to have no effect. Knowing that $I_3 = 0$, there are now only two unknowns, I_1 and I_2 .

Just as in the monostatic measurement case, for the scatterer, $V_2 = -I_2 Z_2$. Substituting for V_2 and I_3 in equation 3.23, and ignoring the first row (the equation relating V_1 to the respective currents) of the equation—only two equations are needed for two unknowns—equation 3.23 becomes

$$\begin{bmatrix} 0 \\ V_3 \end{bmatrix} = \begin{bmatrix} Z_{21} & (Z_{22} + Z_L) \\ Z_{31} & Z_{32} \end{bmatrix} \begin{bmatrix} I_1 \\ I_2 \end{bmatrix} \quad (3.24)$$

By using Cramer's rule to solve for the currents [19]

$$I_1 = \frac{\begin{vmatrix} 0 & (Z_{22} + Z_L) \\ V_3 & Z_{32} \end{vmatrix}}{\begin{vmatrix} Z_{21} & (Z_{22} + Z_L) \\ Z_{31} & Z_{32} \end{vmatrix}} \quad (3.25)$$

Solving for the determinants, V_3 can be solved in terms of the current, I_1 , to give

$$V_3 = \left[Z_{31} - \frac{Z_{21}Z_{32}}{Z_{22} + Z_L} \right] I_1 \quad (3.26)$$

A comparison of equation 3.26 with equation 3.9 reveals that the forms of these equations are quite similar. If the receiving antenna is replaced by the transmitting antenna—in other words the receiving antenna's position equals the transmitting antenna's position—the mutual impedance Z_{32} becomes Z_{12} , and then equation 3.26 is equal to equation 3.9.

For the system without the scatterer present, $V_3^0 = I_1 Z_{31}^0$. Subtracting this from equation 3.26 will show the effect on V_3 as a result of the presence of the scatterer. This is equal to

$$V_3 - V_3^0 = \Delta V_3 = \left[\Delta Z_{31} - \frac{Z_{21}Z_{32}}{Z_{22} + Z_L} \right] I_1 \quad (3.27)$$

where $\Delta Z_{31} = Z_{31} - Z_{31}^0$. Z_{31} represents the mutual impedance for the direct signal between the transmitter and receiver. It is given by $Z_{31} = \frac{V_{31}}{I_1} \Big|_{I_2=I_3=0}$. Z_{31} is not affected by the modulation of the probe, but it is affected by the orientation and position of the probe. If mechanical modulation is used, this will have an effect on the measurements made. Modulation of the probe using electrical methods or modulation using photosensitive devices, will minimize this effect. It can then be assumed that ΔZ_{31} is insignificant in equation 3.27 [2]. Because ΔZ_{31} vanishes, the direct signal will be considerably larger than the modulated signal.

The other mutual impedances can be calculated as follows: $Z_{21} = \frac{V_{21}}{I_1} \Big|_{I_2=I_3=0}$, $Z_{32} = \frac{V_{32}}{I_2} \Big|_{I_1=I_3=0}$ and $Z_{22} = \frac{V_2}{I_2} \Big|_{I_1=I_3=0}$. In these equations, Z_{21} and Z_{32} are the

mutual impedances representing transmission from the transmission antenna to the scatterer and reradiation from the scatterer to the receiving antenna. Reciprocity is not required and cannot be used here. Z_{22} is the self impedance of the scatterer.

3.6 Conclusion

From the theory it is clear that the voltage measured at the receiving antenna—for the monostatic setup—is directly proportional to the square of the electric field incident on the dipole scatterer, should the scatterer be absent. This results from using the Lorentz reciprocity theorem.

The bistatic measurement setup is more complex. The result here was not written in terms of the electric field, but is a function of the impedances. These impedances can be solved in terms of equation 3.12, which are functions of the E-fields and currents.

Chapter 4

Signals and Waves in the System

The general theory needed for the analysis of the system is given here. This includes modulation, noise, quantization, correlation and the detection scheme for the detection of the voltage at the receiving antenna and thus the electric field.

4.1 Amplitude Modulation

Because the scatterer is modulated at its centre with a phototransistor, the scattered signal will be modulated. To have a better understanding of the wave types associated with the modulated scatterer system, a brief overview will be given on amplitude modulation.

There are two types of amplitude modulation: suppressed carrier modulation and large carrier modulation [20]. Suppressed carrier modulation is also called linear modulation, but is not of interest here [21]. With large carrier amplitude modulation (AM), a DC-bias is added to the modulating signal, which results in the carrier signal being rather prominent. The AM-signal is presented mathematically as [20, 21]

$$X_{AM}(\tau) = \alpha_c [1 + mF(\tau)] \cos(\omega_c \tau) \quad (4.1)$$

where α_c is the amplitude of the carrier signal, m is the modulation index, given by

$$m = \frac{\beta_m}{\alpha_c} \quad (4.2)$$

ω_c is the carrier frequency, and τ the time in seconds. β_m is the amplitude of the modulating signal, $F(\tau)$. $F(\tau)$ is normalized so that the maximum value of $|F(\tau)|$ is unity. For the signal to be a large carrier signal, the condition

$$\alpha_c \geq |\min \{\beta_m F(\tau)\}| \quad (4.3)$$

must hold true. If this condition is not satisfied, the detection process will be influenced.

Figure 4.1 shows an example of AM-modulation. The frequency spectrum is found by taking the Fourier transform of the time domain signals over the interval $0 \leq \tau \leq 1.5$ ms. This explains the spectral broadening.

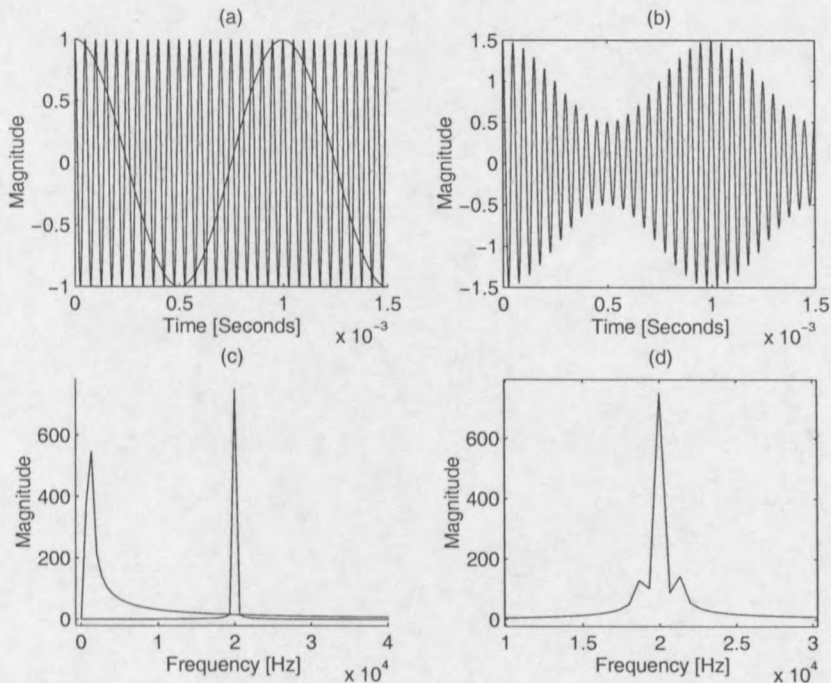


Figure 4.1: Voltage and frequency spectrum for AM-modulation: **(a)** Carrier and modulating signals with parameters: $\omega_c = 20$ kHz, $F(\tau) = \cos(\omega_m \tau)$, $\omega_m = 1$ kHz **(b)** AM-modulated signal with parameters: $\alpha_c = 1$, $m = 0.5$ **(c)** Frequency spectrum of (a). The 1 kHz and 20 kHz signals are clearly visible. **(d)** Frequency spectrum of the AM-signal. The signals at 19 kHz and 21 kHz are just visible in the sidelobes of the main 20 kHz carrier signal.

In both cases of amplitude modulation, synchronous detection can be used to demodulate the signal. However, in the case of large carrier modulation,

it is possible to detect the signal with envelope detection, given that enough power is transmitted. This detection scheme has a few drawbacks, however. The method fails for poor signal-to-noise ratios [20], the DC-response is lost, and the method will cause distortion if the modulating index (equation 4.2) is greater than unity. For the modulating scatterer method, a special kind of synchronous detection will be used.

The fraction of the power in the sidebands, is given by dividing the power of the modulating signal by the total power of the AM-signal [20]

$$\mu = \frac{\overline{\beta_m F^2(\tau)}}{\alpha_c^2 + \overline{\beta_m F^2(\tau)}} \quad (4.4)$$

When $F(\tau)$ is a single sinusoid, equation 4.4 reduces to

$$\mu = \frac{\beta_m^2}{2 + \beta_m^2} \quad (4.5)$$

For $\beta_m \leq 1$, the best efficiency of the system is 33%. Therefore, for the modulated scatterer method, it is very important to have the highest possible modulation index.

4.2 Noise

Noise interferes with the measurements that are made. It is therefore important to consider the noise (and the properties of noise) that may be expected in the modulated scatterer system.

4.2.1 Noise Bandwidth

Every linear system has a noise bandwidth which can be defined as [21, 22]

$$B_n = \frac{1}{2\pi} \frac{\int_0^\infty |H(\omega)|^2 d\omega}{|H(\omega_0)|^2} \quad [\text{Hz}] \quad (4.6)$$

In the above equation, B_n is the noise bandwidth, and $H(\omega)$ is the transfer function of the system under consideration (whether band pass, low pass or high pass). ω_0 is the centerband frequency.

It will be shown in section 4.3.2 that, by narrowing the bandwidth of a system, the signal to noise ratio can be improved. This is a very easy way of dropping the noise floor.

4.2.2 White Noise

White noise is noise that uniformly covers the entire spectrum [21, 22]. With a constant power spectral density of η watts per Hertz (measured over positive frequencies), the power spectral density of white noise is

$$S_n(\omega) = \frac{\eta}{2} \quad [\text{W/Hz}] \quad (4.7)$$

for all ω . The factor of $\frac{1}{2}$ is necessary for two-sided spectral density [20]. If S_n is multiplied with a resistor value, R , a mean-square voltage will be obtained.

No system has infinite bandwidth, therefore the power of the noise in a given bandwidth B , is

$$\begin{aligned} P_n &= \frac{1}{2\pi} \int_{-2\pi B}^{2\pi B} \left(\frac{\eta}{2}\right) d\omega \\ &= \eta B \quad [\text{W}] \end{aligned} \quad (4.8)$$

4.2.3 Thermal Noise

Thermally excited random motion of free electrons in a conducting or semi-conducting medium, is a source of noise called thermal noise, which closely resembles white noise. The mean value of thermal noise is zero. For normal frequencies below the optical range and normal temperatures [23], or where $|\omega| \ll \frac{2\pi kT}{h}$, the power spectral density of thermal noise is given by [20]

$$S_n(\omega) \cong 2kT \quad [\text{W/Hz}] \quad (4.9)$$

T is the temperature of the medium, k is Boltzmann's constant and h is Planck's constant. Substituting equation 4.9 into equations 4.7 and 4.8 gives a noise power of

$$P_n = 4kTB \quad [\text{W}] \quad (4.10)$$

4.2.4 Noise Figure

Consider any system with a bandwidth B and a gain of G , which is matched to a resistance R at room temperature, T_0 . The system's noise figure is then defined as [23]

$$\begin{aligned}
 F &= \frac{\text{SNR at input}}{\text{SNR at output}} \\
 &= \frac{P_{si}/kT_0B}{GP_{si}/(GkT_0B + P_{na})} \\
 &= 1 + \frac{P_{na}}{GkT_0B}
 \end{aligned} \tag{4.11}$$

with P_{si} the input signal power, and P_{na} the additional noise power added by the system.

4.2.5 Noise Temperature

The available noise power from a thermal noise source is the maximum thermal noise power that can be extracted from a noisy resistor, and is given by

$$P_L = kTB \tag{4.12}$$

The available noise power will be extracted when the load resistor is equal to the noisy resistor. The noise temperature specifies the thermal noise power into a matched resistance.

The equivalent noise temperature of a system, T_e , is the effective temperature of a white thermal noise source at the system input that would be required to produce the same noise power at the output of an equivalent noiseless system.

As an example from section 4.2.4, equation 4.11, it is easy to see that the noise contributed by the system can be expressed as

$$P_{na} = G(F - 1)kT_0B \tag{4.13}$$

From the definition of noise temperature, and equations 4.12 and 4.13, the noise temperature of the system, T_s , can be seen to be

$$T_s = (F - 1)T_0 \quad (4.14)$$

4.2.6 Noise in Cascaded Systems

If a system consists of a series of cascaded smaller systems, each with a noise figure of F_1, F_2, \dots, F_N and gains of G_1, G_2, \dots, G_N respectively, the total noise figure of the cascaded system can be shown to be [23]

$$F_T = F_1 + \frac{F_2 - 1}{G_1} + \frac{F_3 - 1}{G_1 G_2} + \dots + \frac{F_N - 1}{G_T} \quad (4.15)$$

where it was assumed that the cascaded system's impedances were all matched. The noise added by the system can then be calculated with the aid of equation 4.13.

4.2.7 Antenna Noise Temperature

Because of the existence of electromagnetic radiation, all antennas produce noise at their outputs. In the vicinity of the X-band, 8 GHz to 12 GHz, the noise sources are more galactic [20]. Therefore, taking the noise temperature equal to the ambient temperature, in an anechoic chamber, is appropriate. Just as in the case of a system, the noise temperature of an antenna is that temperature by which a noise source should be to supply an equivalent amount of noise, should the antenna be noiseless.

4.2.8 Quantization Noise

Because an analog to digital converter is used, an overview will be given of quantization noise. Quantization is the process where a sample is taken from a signal and the amplitude of the sample is represented in a finite number of digits (a digital number). The error introduced is called a quantization error or quantization noise [24].

Let $X_a(\tau)$ be an analog signal with a maximum value of $X_{a_{max}}$ and a minimum value of $X_{a_{min}}$. The span of the signal will be the maximum value minus the minimum value, and is denoted by S_a . $X_a(\tau)$ is sampled at time intervals $n\Delta\tau$ and becomes $X_d(n)$. Let $Q(x)$ be a quantization function,

then the quantized signal is $X_q(n) = Q[X_d(n)]$. The quantization error is now given as

$$e_q(n) = X_q(n) - X_d(n) \quad (4.16)$$

Let Δ be the quantization step size, defined as

$$\Delta = \frac{X_{a_{max}} - X_{a_{min}}}{2^b - 1} \quad (4.17)$$

where b is the number of bits in the converter, then the error must satisfy the following equality

$$-\frac{\Delta}{2} \leq e_q(n) \leq \frac{\Delta}{2} \quad (4.18)$$

The maximum error is then $\frac{\Delta}{2}$. The power as a result of the error has to be calculated. This is done by [24]

$$P_q = \frac{1}{2\tau} \int_{-\tau}^{\tau} e_q^2(t) dt = \frac{1}{\tau} \int_0^{\tau} e_q^2(t) dt \quad (4.19)$$

with $e_q(t) = \left(\frac{\Delta}{2\tau}\right)t$ and $-\tau \leq t \leq \tau$. Here it was assumed that the function $X_a(\tau)$ is linear over $-\Delta\tau/2$ and $\Delta\tau/2$ so that the error could be approximated by a linear function. Substituting $e_q(t)$ into equation 4.19 gives a total power for the quantization error as

$$P_q = \frac{\Delta^2}{12} \quad (4.20)$$

Δ (equation 4.17) can be approximated if the number of bits is large enough, so that Δ becomes

$$\Delta \approx \frac{S_a}{2^b} \quad (4.21)$$

where S_a was substituted for $(X_{a_{max}} - X_{a_{min}})$. The more bits used, the smaller the error in the approximation. Equation 4.21 can be substituted in equation 4.20 which simplifies to

$$P_q = \frac{S_a}{12 \cdot 2^{2b}} \quad (4.22)$$

4.3 Signal-to-Noise Ratio

The signal-to-noise ratio (SNR) is a dimensionless ratio of signal power to noise power

$$SNR = \frac{\overline{S^2(\tau)}}{\overline{n^2(\tau)}} \quad (4.23)$$

where $\overline{S^2(\tau)}$ and $\overline{n^2(\tau)}$ are the power of the signal and noise respectively.

4.3.1 Signal-to-Noise Ratio in Amplitude Modulation

The mathematical description for AM was given in equation 4.1. If the signal is demodulated with a synchronous detector, the output of the demodulator will be

$$Y(\tau) = \frac{\alpha_c m F(\tau)}{2} + n_c(\tau) \quad (4.24)$$

where the synchronous demodulator signal was taken as $\cos(\omega_c \tau)$ and the noise $n_c(\tau) = n(\tau) \cos(\omega_c \tau)$. The AM-signal power after modulation is easily evaluated as

$$S_D = \left(\frac{\alpha_c m}{2} \right)^2 \overline{F(\tau)^2} \quad (4.25)$$

and the noise power is

$$N_D = \overline{n_c(\tau)^2} = 2\eta B \quad (4.26)$$

Before detection, the signal power is

$$S_T = \frac{1}{2} \alpha_c^2 + \frac{1}{2} \alpha_c^2 m^2 \overline{F(\tau)^2} \quad (4.27)$$

The noise power is the same as in equation 4.26. These equations result in a detection gain, given by

$$\frac{SNR_D}{SNR_T} = \frac{m^2 \overline{F(\tau)^2}}{2 + 2m^2 \overline{F(\tau)^2}} \quad (4.28)$$

4.3.2 Improving the Signal-to-Noise Ratio

If the bandwidth of the signal is limited to a bandwidth B , the signal-to-noise ratio can be improved.

Let the signal have a finite power of P_T watt. Noise is added to the signal with double-sided power spectral density, $\frac{\eta}{2}$ W/Hz, and a bandwidth B . This gives a total noise power of $P_n = \eta B$ according to equation 4.8. The signal-to-noise ratio is therefore

$$SNR = \frac{P_T}{\eta B} \quad (4.29)$$

By limiting the bandwidth of the noise to W Hz, the signal-to-noise ratio becomes

$$SNR = \frac{P_T}{\eta W} \quad (4.30)$$

It is clear from equations 4.29 and 4.30 that the signal-to-noise ratio can be improved by $\frac{B}{W}$ by limiting the bandwidth of the system.

Another way of improving the signal-to-noise ratio of a measurement, is by making use of averaging. Because the mean value of noise is zero, the effect of noise can be minimized. In mathematical terms, this can be equated as

$$\lim_{N \rightarrow \infty} \sum_{k=0}^N n(k) = 0 \quad (4.31)$$

where $n(k)$ was taken as the sampled noise. In general, for uncorrelated noise with a zero mean, the noise floor will drop a factor which is equal to the averaging factor [25, 26].

4.4 Correlation

When two analog signals are mixed, they are in effect multiplied (for example in a synchronous detector). Therefore, the mathematical model of frequency mixing can be simplified to pure multiplication. Take for example two analog signals, $f(\tau)$ and $g(\tau)$. Their product would be

$$h(\tau) = f(\tau) \cdot g(\tau) \quad (4.32)$$

Transferring this operation to the frequency domain, it is seen that the frequencies are convolved.

4.4.1 The Mathematical Model of Correlation

By sampling the analog signals, at intervals $n\Delta\tau$, the signals can be transferred to the digital domain. $f(\tau)$ and $g(\tau)$ then become $f(n)$ and $g(n)$. The definition of cross-correlation for discrete-time, energy signals is given as [24]

$$\begin{aligned} R_{fg}(l) &= \sum_{n=-\infty}^{\infty} f(n)g(n-l) \\ &= \sum_{n=-\infty}^{\infty} f(n+l)g(n) \end{aligned} \quad (4.33)$$

The parameter l is a time shift. It results in one of the signals being shifted in time with respect to the other. For autocorrelation—the correlation between the signal and itself— $g(n)$ is replaced by $f(n)$. When finite sequences are used, as in physical experiments, it is not possible to use equation 4.33. It then becomes

$$R_{fg} = \sum_{n=i}^{N-|k|-1} f(n)g(n-l) \quad (4.34)$$

In equation 4.34, N is the length of the sequences $f(n)$ and $g(n)$, $i = l$ and $k = 0$ for $l \geq 0$, and $i = 0$ and $k = l$ for $l < 0$.

For power signals, $f_p(n)$ and $g_p(n)$, the cross-correlation sequence is modified to

$$R_{fg}(l) = \lim_{M \rightarrow \infty} \frac{1}{2M+1} \sum_{n=-M}^M f(n)g(n-l) \quad (4.35)$$

4.4.2 Correlation used in the Modulated Scatterer System

In the application of radar or sonar, correlation is used to detect the incoming signal and the delay in the signal. By shifting one of the signals, the

correlation sequence will have a peak when the two signals are in phase. At this peak point, the parameter l will give the difference in the phase of the outgoing and incoming signals.

In the application of the modulated scatterer technique, the difference between the incoming and the reference signal will be infinitesimal, because of the very large wavelength of the modulating signal.* It is therefore known that the correlation sequence will peak at l equals zero. In the modulated scatterer technique, the question is one of amplitude. The zero phase correlation ($l = 0$) of the constant amplitude reference signal and varying scattered signals will give a value proportional to the amplitude of the scattered signals. Equation 4.34 can be written for this specific case as

$$V_S = \sum_{n=0}^N S(n)R(n) \quad (4.36)$$

where V_S is the amplitude of the signal at the output of the detector due to the modulated scatterer, $S(n)$ is the sampled signal at the output of the detector (consisting of the wanted signal and unwanted noise), and $R(n)$ is the modulating, reference signal. N is the total number of samples taken. From section 4.3.2, it is clear that the more samples taken, the more accurate V_S will be.

4.5 Detailed Detection Scheme

The main idea is to extract the amplitude and phase information from the measured V_s in equation 3.17. This is done by IQ-detection, or in-phase quadrature-phase detection. It is evident from figure 2.3 that, because of the high frequency at which we are measuring (10 GHz), it is very difficult to have equal paths for the LO (local oscillator) and RF (the scattered wave—the backward wave in the source antenna) sides of the mixers. This error can be removed with calibration.

The LO signal is taken as a pure sinus wave. It will be split by a hybrid coupler to give a 0° and a 90° signal. For the general case, the LO signal is given by

$$LO = \alpha \cos(\omega_t \tau + \theta) \quad (4.37)$$

*For a modulating signal between 1 kHz and 10 kHz, the wavelength will be between 30 km and 300 km.

The dipole is switched with the low frequency signal as explained earlier. This is equal to a low frequency signal that is amplitude modulated and can be expressed as follows

$$RF = \alpha[\epsilon + m \cos(\omega_m \tau)] \cos(\omega_t \tau + \phi) \quad (4.38)$$

In these equations, ω_t is the frequency of the transmitted wave, ω_m is the frequency of the scattered (modulated) wave. θ and ϕ are the angles of the LO and RF signals respectively, at the detector input and τ is time in seconds. The modulation constant, m , is given by

$$m = \frac{\beta}{\alpha} \quad (4.39)$$

so that $\alpha m = \beta$ in equation 4.38.

The IF signal is at the output of the detector, and is the product of the RF and LO signals. Multiplying these signals gives

$$\begin{aligned} IF &= \frac{\alpha^2 \epsilon}{2} [\cos(2\omega_t \tau + \theta + \phi) + \cos(\theta - \phi)] \\ &\quad + \frac{\alpha \beta}{4} [\cos(2\omega_t \tau + \omega_m \tau + \theta + \phi) \\ &\quad + \cos(2\omega_t \tau - \omega_m \tau + \theta + \phi) \\ &\quad + 2 \cos(\theta - \phi) \cos(\omega_m \tau)] \end{aligned} \quad (4.40)$$

Equation 4.40 includes high frequency components. By using a low pass filter, unwanted frequencies are filtered out, leaving us with only the lower DC and 10 kHz signals. It is worthwhile to note that this is not a loss of valuable power. The power from the modulated signal is preserved. It is only the power components from unwanted scatterings that are filtered out. Equation 4.40 becomes

$$IF = \frac{\alpha^2 \epsilon}{2} \cos(\theta - \phi) + \frac{\alpha \beta}{2} \cos(\theta - \phi) \cos(\omega_m \tau) \quad (4.41)$$

The IQ-demodulator produces two signals, a 0° and 90° version. Setting θ in equation 4.41 equal to 0° and 90° respectively, gives the following output

$$\begin{aligned}
 V_{0^\circ} &= \frac{\alpha^2 \epsilon}{2} \cos(\phi) + \frac{\alpha \beta}{2} \cos(\phi) \cos(\omega_m \tau) \\
 V_{90^\circ} &= \frac{\alpha^2 \epsilon}{2} \sin(\phi) + \frac{\alpha \beta}{2} \sin(\phi) \cos(\omega_m \tau)
 \end{aligned} \tag{4.42}$$

The outputs of the IQ-demodulator consists of a DC component plus a component at 10 kHz. The components at DC are the result of scatterings from areas other than the modulated scatterer, which in turn produces the 10 kHz component. Filtering out the DC component, equation 4.42 becomes

$$\begin{aligned}
 V_{0^\circ} &= \frac{\alpha \beta}{2} \cos(\phi) \cos(\omega_m \tau) \\
 V_{90^\circ} &= \frac{\alpha \beta}{2} \sin(\phi) \cos(\omega_m \tau)
 \end{aligned} \tag{4.43}$$

Using only the maximum values of equation 4.43 and realizing that (see figure 4.2)

$$V_s = V_{0^\circ} + jV_{90^\circ} \tag{4.44}$$

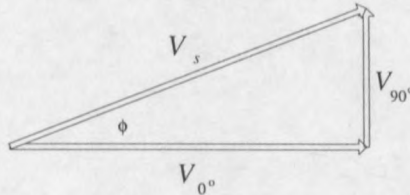


Figure 4.2: The components of vector V_s .

equation 3.17 can be used to calculate the E-field at the position of the probe. If we take E as the amplitude of the electric field, and φ as the phase, we find from equation 3.17 and 4.44 that

$$\begin{aligned}
 E &= \sqrt{\frac{1}{k}} \left(\sqrt{V_{0^\circ}^2 + V_{90^\circ}^2} \right)^{\frac{1}{2}} \\
 \varphi &= \frac{\phi}{2}
 \end{aligned} \tag{4.45}$$

4.6 Mechanical Modulation

The general case for mechanical modulation will be given here. It will be assumed that the field is elliptically polarized, as in figure 4.3, with an x - and y -component. It will be shown that the modulation frequency is double the rotation frequency.

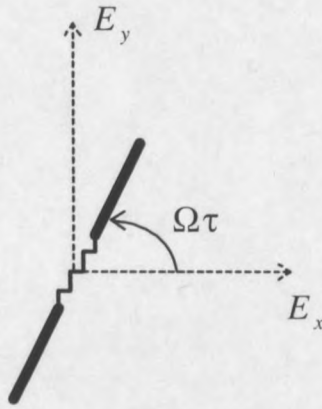


Figure 4.3: Mechanically modulated probe in an elliptical E-field.

The electric field component, \mathbf{E}_x , has vector $\boldsymbol{\eta}_x$, and \mathbf{E}_y has vector $\boldsymbol{\eta}_y$. The x -directed field will contribute a $\cos(\Omega\tau)$ -component, while the y -directed field will contribute a $\sin(\Omega\tau)$ -component. Therefore, along the dipole, the parallel vector $\boldsymbol{\eta}_\rho$ will take the form

$$\boldsymbol{\eta}_\rho = \boldsymbol{\eta}_x \cos(\Omega\tau) + \boldsymbol{\eta}_y \sin(\Omega\tau) \quad (4.46)$$

The field on the probe will be the sum of the two components, \mathbf{E}_x and \mathbf{E}_y , along the length of the dipole, with vector $\boldsymbol{\eta}_\rho$. The field on the probe is therefore given by

$$\boldsymbol{\eta}_\rho \cdot \mathbf{E}_\rho = \mathbf{E}_x \cos(\Omega\tau) + \mathbf{E}_y \sin(\Omega\tau) \quad (4.47)$$

It was stated in section 3.2 that the backscattered signal in the receiver antenna was of the form $\beta = \alpha k (\boldsymbol{\eta} \cdot \mathbf{E})^2$, where \mathbf{E} is the E-field at the position of the probe. Combining this and equation 4.47, the backscattered signal in the receiver antenna is proportional to

$$\begin{aligned}
 (\boldsymbol{\eta}_\rho \cdot \mathbf{E})^2 &= E_x^2 e^{j2\phi_x} \cos^2(\Omega\tau) + \\
 & 2E_x E_y e^{j(\phi_x + \phi_y)} \cos(\Omega\tau) \sin(\Omega\tau) + \\
 & E_y^2 e^{j2\phi_y} \sin^2(\Omega\tau)
 \end{aligned} \tag{4.48}$$

Other unwanted, unmodulated components of the form $\cos(\omega_t\tau + \xi)$ will also add to the backscattered signal. These can be ignored, because it will result in DC-components in the output of the detector, which will be filtered out.

Simplifying equation 4.48 with known trigonometric identities[†], the equation becomes

$$\begin{aligned}
 (\boldsymbol{\eta}_\rho \cdot \mathbf{E})^2 &= \frac{E_x^2}{2} e^{j2\phi_x} [\cos(2\Omega\tau) + 1] + \\
 & E_x E_y e^{j(\phi_x + \phi_y)} \sin(2\Omega\tau) + \\
 & \frac{E_y^2}{2} e^{j2\phi_y} [1 - \cos(2\Omega\tau)]
 \end{aligned} \tag{4.49}$$

From this equation it is easy to see that the modulation frequency is double the rotation frequency, Ω . For detection purposes, the LO-signal can again be taken as the signal in equation 4.37. The detection of the signal in the receiver antenna, is done in the same way as in section 4.5, and will not be done here.

Extracting the amplitude and phase information for the different components, is a tedious procedure. The measurement procedure is rather complex, because there are four unknowns to be determined. A complete procedure for measuring the four unknowns, was suggested by [7]. Further detail can be found in [2].

[†] $\cos^2(\chi) = \frac{1}{2} \cos(2\chi) + \frac{1}{2}$
 $\sin^2(\chi) = \frac{1}{2} - \frac{1}{2} \cos(2\chi)$
 $\sin(2\chi) = 2 \sin(\chi) \cos(\chi)$

Chapter 5

Sensitivity Analysis

A sensitivity analysis has been done for the configuration of figure 5.1, with the critical component values specified in table 5.1. It is important to note that the radar equation cannot be used, since measurements are made in the near field.

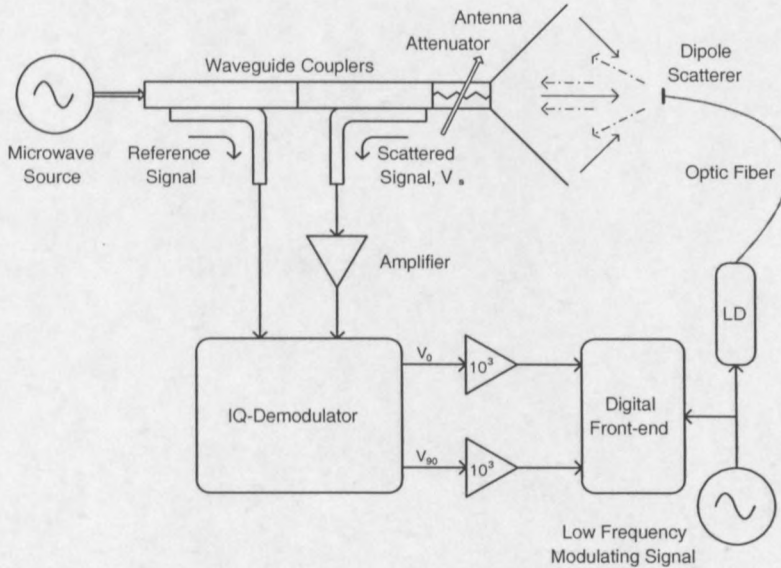


Figure 5.1: Detailed configuration used for the sensitivity analysis.

5.1 Analysis of the System Sensitivity

A SNR approach will be taken here. The noise power at the microwave amplifier's input, with origin from the antenna, is given by [23]

$$P_n = k\Delta f \frac{T_A + (L - 1)T}{L} \quad (5.1)$$

where P_n is the power delivered to the amplifier, k is Boltzmann's constant (1.38×10^{-23} J/K), Δf is the bandwidth in which the noise is observed (taken as 10 kHz, the bandwidth of the receiver), T is room temperature in Kelvin (290 K), T_A is the antenna noise temperature (taken as 300 K: measurements are made in an anechoic chamber, so this will represent black body radiation from the absorbing material), and L is the loss from the antenna to the mixer (for a very short length, it is taken as 2 dB). These parameters give the noise power from the antenna and surroundings as $P_n = -162$ dB.

For a cascaded system, the total noise figure is [23]

$$F_T = F_1 + \frac{F_2 - 1}{A_1} + \frac{F_3 - 1}{A_1 A_2} + \dots + \frac{F_N - 1}{A_T} \quad (5.2)$$

If we take all the components to be noiseless, the noise referred to the input of the microwave amplifier will be

$$P_{nc} = kT_0\Delta f \cdot \left[F_{amp} - 1 + \frac{F_{mixer} - 1}{A_{amp}} + \frac{F_{IFamp} - 1}{A_{amp} A_{loss}} \right] \quad (5.3)$$

where the symbols take their normal meaning. A_{loss} is the absolute value of

Table 5.1: Component specifications

Component	Gain dB	Noise Figure dB
Microwave Amplifier	10	1.5
Mixer	-7	7.5
Audio Amplifier	30	10

the conversion loss of the mixer (table 5.1 gives the gain of the mixer as -7, a loss of 7 dB). Solving for this equation, gives $P_{amp} = -156$ dB. Adding P_{nc} to P_n from equation 5.1, gives a total noise power at the mixer input of -156 dB.

An analog to digital converter and a computer is used to measure the amplitude and phase information from the IQ-demodulator. The AD-converter introduces a quantization error. If the quantizer has an accuracy of β bits, the mean-square error power is given by

$$P_q = \frac{\alpha^2}{3 \times 2^{2\beta}} \quad (5.4)$$

where α is the span of the AD-converter.

According to the datasheets of the PCM1800 [27], stereo AD-converter, the maximum swing is equal to $2.828 V_{p-p}$. Using equation 4.17 or 4.21, $\Delta = 2.697 \times 10^{-6}$ V, and equation 5.4, $P_q = -122$ dBW. This is indeed very small. Although the different equations suggests that a signal with amplitude of -122 dBW can be measured, the datasheets specify a dynamic range of -95 dBV*. Given that the signal is amplified with a 30 dB amplifier prior to detection, it is safe to assume that, with this system, a signal in the order of -125 dBV at the antenna could be measured. In a 50Ω system, this is equal to -110 dBm†. For a 16 bit system, $\Delta = 43.15 \times 10^{-6}$ V and $P_q = -92$ dBW. This is an approximate dynamic range of -120 dBV, including the 30 dB amplification, which equals to -107 dBm in a 50Ω system.

5.2 Measurement of the Linearity

To measure the sensitivity of the system, the probe was placed in the mouth of the horn, at the waveguide opening. The power delivered to the antenna was attenuated in steps of 3 dB, at the feed point of the antenna. The field was then measured in the way described in section 6.3. Because the variable attenuator reduced both the transmitted and received signals, the backscattered field would be 6 dB smaller for every additional 3 dB attenuation.

According to the reciprocity theorem, and in effect equation 3.22, the field measured should be linearly decreasing in steps of 3 dB and not in steps of 6 dB as one would start to think. This is in contrast with the voltage

* dBV = $20 \log\left(\frac{V}{1 \text{ volt}}\right)$

†The RMS value of the voltage was assumed.

measured at the detector, which is decreasing in steps of 6 dB for every 3 dB attenuation. Table 5.2 shows an example of the magnitudes of the different parameters.

Table 5.2: Measurement of the linearity: an example

Attenuation dB	E V/m	E dB	E ² V ² /m ²	E ² dB	Measured V volt	Measured V dB
0	1	0	1	0	1	0
3	$\frac{1}{\sqrt{2}}$	-3	$\frac{1}{2}$	-6	$\frac{1}{2}$	-6
6	$\frac{1}{2}$	-6	$\frac{1}{4}$	-12	$\frac{1}{4}$	-12

The power of the microwave source at the input of the attenuator, was about 13 dBm. The power at the output of the antenna—attenuated power—would thus be between 13 dBm and -35 dBm. The results of this measurement can be seen in figure 5.2. The error of measurement at each point was calculated and can be seen in figure 5.3. The error was throughout less than 1.2% and the measurements were quite linear. The sensitivity measurement is in good agreement with work done by [1].

The first point saturated the detector, because of the strong reflections. This can be overcome by decreasing amplification of the IF signal.

5.3 Calculations on Sensitivity Measurements

To find the fields inside a waveguide, the orientation of the axes are as in figure 5.4.

The complete analysis of the waveguide structure can be found in many textbooks [16, 14], and it will not be repeated here. Only the equations will be used.

The impedance of the waveguide for the TE-mode, is given by

$$Z_{TE} = \frac{\eta}{\sqrt{1 - \left(\frac{\lambda}{2a}\right)^2}} \quad (5.5)$$

where η is the wave impedance in free space, and is equal to 377 Ω . For the TE₁₀ mode, the E-field in a waveguide along the x-axis is given by

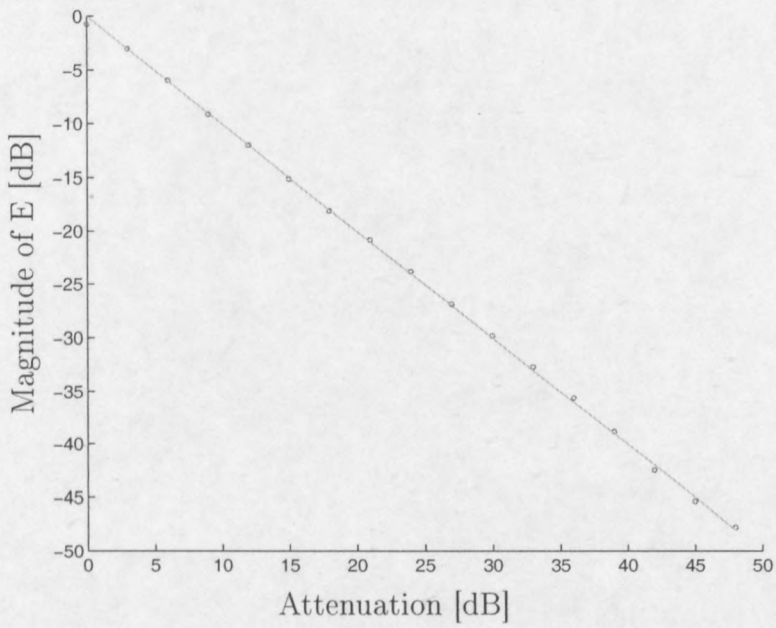


Figure 5.2: Measurement of the system linearity.

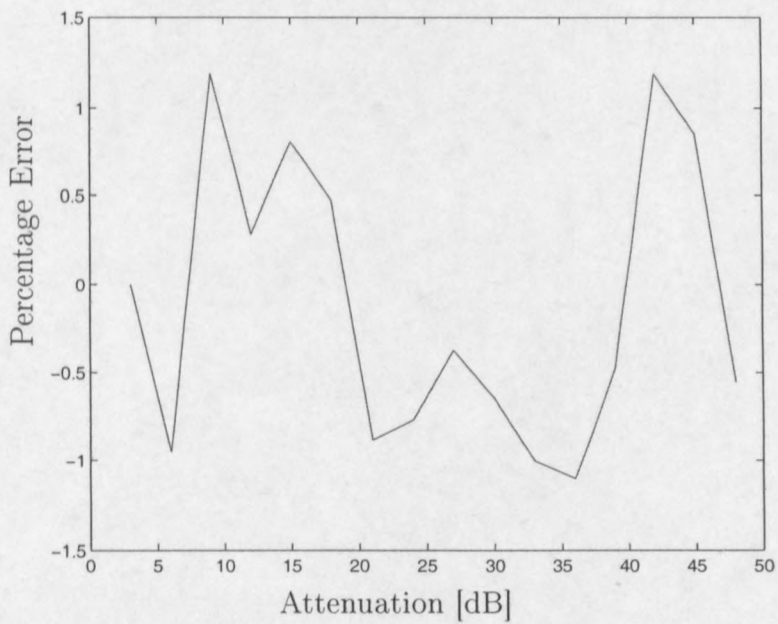


Figure 5.3: Error in the linearity measurement.

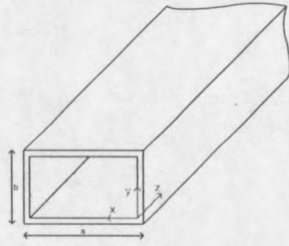


Figure 5.4: X-band waveguide.

$$E = E_m \sin\left(\frac{\pi x}{a}\right) \quad (5.6)$$

so that the average power in the waveguide (in the xz -plane) is equal to

$$P_{Avg} = \frac{E_m^2}{2Z_{TE}} \quad (5.7)$$

With the attenuator set to 0 dB, there is approximately 13 dBm of power transmitted by the horn antenna. This is equal to approximately 86 W/m^2 in the mouth of the horn. The average power incident on the dipole probe is therefore approximately $357 \mu\text{W}$ (-5 dBm). The dipole scatters omnidirectionally. Half of the power radiates back towards the receiver, while the other half radiates into space.

If it is assumed that the modulation of the dipole is such that the difference in the power scattered is a hundredth (-20 dB) of the total power, -28 dBm of power radiates back toward the receiver. The backscattered signal is coupled through a 3 dB waveguide coupler, therefore, only -31 dBm reaches the waveguide to coaxial converter. With a 500Ω impedance in the waveguide, and the coaxial lines only 50Ω , there is a reflection of about 7.5 dB. The power that reaches the amplifier is approximately -39 dBm. The signal is amplified by 10 dB. The signal is further split by the hybrid coupler into two signals with equal power and mixed with the LO-signal. Further losses, like the conversion loss in the mixers, are in the order of 15 dB. The result is a signal with a power of approximately -47 dBm at the receiver. In a 50Ω system, this results in a voltage of approximately 1 mV. By amplifying this by a factor of 1000, the voltage measured is in the order of 1 V peak. This was the approximate voltage sampled by the AD-converter during the specific measurement.

If the same reasoning is followed for the attenuator set to 48 dB, the signal power at the receiver would be approximately -110 dBm after the 30 dB audio amplification. Here it must be remembered that the backscattered signal is attenuated by the waveguide attenuator. This should be accounted for.

It can be seen that, for the 16 bit system used, the detector operated well according to the theory. Although the limit should have been reached, the detector was still linear after high attenuation. This could be because of the assumption made that only a hundredth of the power is scattered back towards the receiver from the dipole. From the attenuation it is seen that the detector is linear over at least 96 dB.

Chapter 6

Practical Implementation

An overview will be given about the practical implementation of the system.

6.1 The Probe

The probe used was constructed from a phototransistor. Most of the plastic was cut away, so that perturbation would be a minimum. The legs of the transistor was used as the dipole antenna.

The optic fiber was glued to the phototransistor. The constructed probe was covered in a black sleeve to minimize the effect from sunlight.

A diagram of the constructed probe can be seen in figure 6.1.

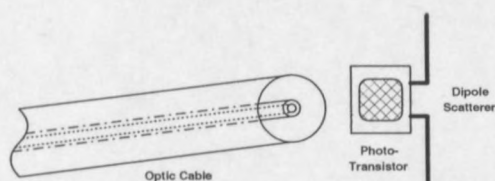


Figure 6.1: Construction of the probe.

A probe with a length of 10.4 mm was used in all the measurements, except the diffraction measurement in section 7.4, where a probe with a length of 15 mm was used and the sensitivity measurement, where an 8.3 mm probe was used. The smaller the probe, the better the resolution. For the measurement of the diffraction the resolution is not that critical, and a probe was

used which gave a bit more sensitivity through resonance.

6.2 IQ-Detector

The in-phase quadrature-phase detector used was built as in figure 6.2.

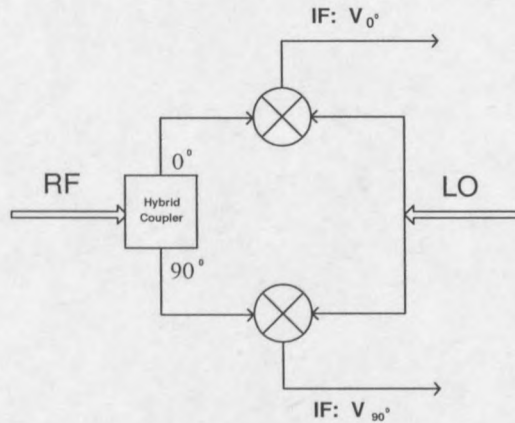


Figure 6.2: IQ-detector construction.

There are a few practical considerations in the design of this detector. The optimal value of the LO-signal will result in the least conversion loss when the signals are mixed. It is thus very important to ensure that the LO-signal is at its optimum level. Before the RF-signal is split with the hybrid coupler, it can be amplified. Care must be taken that the amplified signal power will not exceed the limits of either the coupler or the mixers.

The signals are very small. To measure these signals with an analog to digital conversion process, it is necessary to amplify the IF signals. An audio amplifier was used for this purpose with an amplification of 30 dB.

6.3 Description of the Measurement Setup

Figure 6.3 shows a detailed schematic of the setup used.

The microwave source is a very stable 10 GHz synthesized oscillator. The power delivered to the setup is 17 dBm, which is split with a female sma-type T-junction. The power at the antenna is therefore in the order of 13.5 dBm,

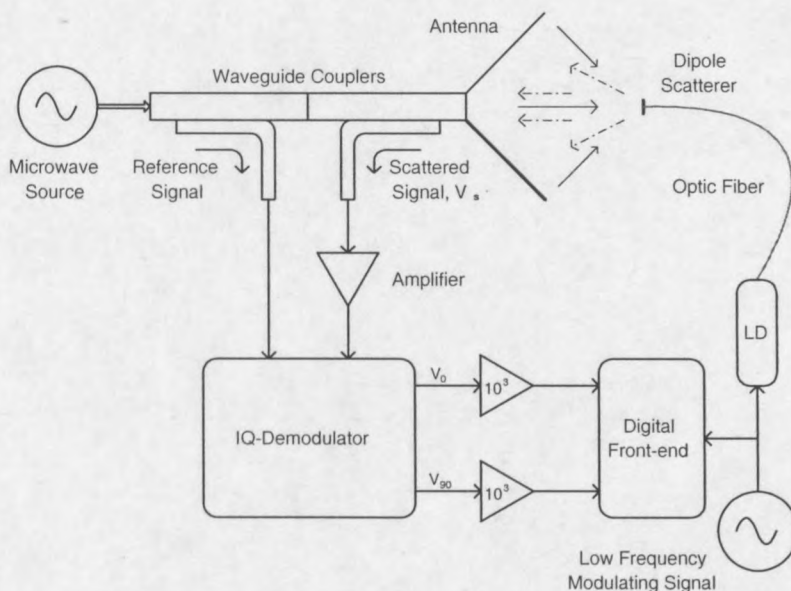


Figure 6.3: Detailed configuration used for the measurements.

because the T-junction is not an ideal power divider. The signal which is used for the LO of the detector is split again using another T-junction, so that each mixer is driven with an LO signal level in the order of 10 dBm.

The backscattered signal is coupled from the backward wave with a 3 dB waveguide coupler. This is to ensure absolute minimum losses. The signal is then amplified with a low noise microwave amplifier. The amplifier has a gain of about 12 dB at 10 GHz [28]. The signal from the amplifier is split by a 90° hybrid coupler and mixed with the LO signal from the source. The IF signals are then amplified by a factor of approximately 30 dB by an audio based amplifier. The two signals, the 0° and 90° phased signals from the audio amplifier, are then measured alternatively and correlated with the reference signal with which the laser is driven. The correlated data represents the amplitude and phase of the field at the position where the probe was placed.

Measurements were made by using the sound card of a computer. It is in effect a 16-bit analog to digital converter. The data was recorded and saved in MATLAB (.mat) format by using the program “GoldWave”.

A standard measurement procedure was derived which works as follows (see figure 6.3):

1. Set the path of the detector to V_0 .

2. Take samples of the signal V_0 and the modulating signal, so that the samples are synchronized in time.
3. Set the path of the detector to V_{90} .
4. Take samples of the signal V_{90} and the modulating signal, so that the samples are synchronized in time.
5. Take a calibration measurement by placing the probe at a position of a known field. To measure the pattern of an antenna, a point may be chosen to represent unity amplitude and zero degree phase, or any other chosen field.
6. Repeat steps 1 to 4 for each of the points to be measured. The data should be stored.
7. Take a measurement without modulation of the probe. It is important to disconnect the optic fiber, and not to shut the modulator off. The goal is to measure the parasitic coupling of the modulating signal with the measurement electronics. It was found to be significant when the measured fields are small. This measurement does not have to be done for each field point. It is done only once, because the coupling stays the same, irrespective of the position of the probe.
8. Process the data and plot the results.

To improve accuracy of measurements, a wooden structure was built to move the probe on the y-axis. The metal plate is optional and was used for the half plane diffraction measurements.

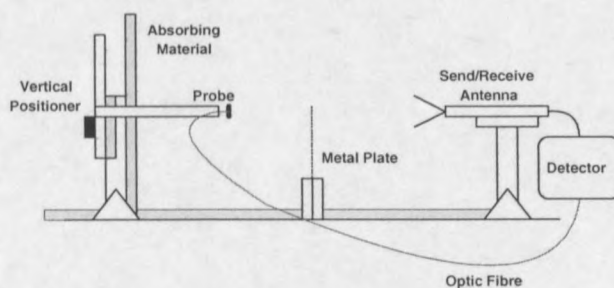


Figure 6.4: Structure used in the measurements.

6.4 Computation of the Field from the Measured Data

Once the data has been collected with the measurement process, it should be processed to extract the electric field information from it. The correlation process was described in section 4.4. This process is used to extract the amplitude from the small modulated signal. This amplitude is then proportional to the square of the electric field incident on the probe.

A number system was adopted in which the field points were numbered. Starting from one, the points were numbered in ascending order. The file-names used for storing the data—each field point's data is stored in two separate files—would then be an alpha numeric filename. The data stored for the zero phased channel of the hybrid would be characterized with “d”, while the 90° channel would be characterized with “jd”. The first point would thus have two files, “d1.mat” and “jd1.mat”, for the V_0 and V_{90} channels respectively. The calibration point was saved as “kal.mat” and “jkal.mat” respectively, while the data without the probe modulated would be saved as “dsp.mat” and “jdsp.mat” respectively. A standard calibration can also be done on a known field and can then be used to calculate absolute field values. The data gathered was sampled at 44.1 kHz, the standard high quality audio sampling rate. For each measurement a total of 441 000 points were sampled, which takes 10 seconds per measurement.

A MATLAB program was written to compute the fields. This program can be found in appendix F.1.

Although this way of measurement is time consuming, automation of the measurement process and in-time computation and storing of the field values with data acquisition equipment, would make this measurement technique extremely fast and effective.

Chapter 7

Practical Measurements

This chapter is dedicated to practical measurements taken with the system. A complete description of the system can be found in section 6.3.

7.1 Pyramidal Horn

The near field of a Marconi pyramidal horn antenna was measured. To have a comparison with the theory, a model was set up in FEKO and simulated. The program code for the FEKO simulation can be found in appendix G.1.

The geometry used for the measurement of the pyramidal horn antenna can be seen in figure 7.1. Measurements were taken on the y -axis at $x = 0$ and $z = 0.002$ meter.

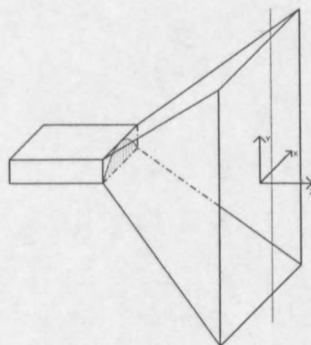


Figure 7.1: Geometry of the pyramidal horn antenna measured.

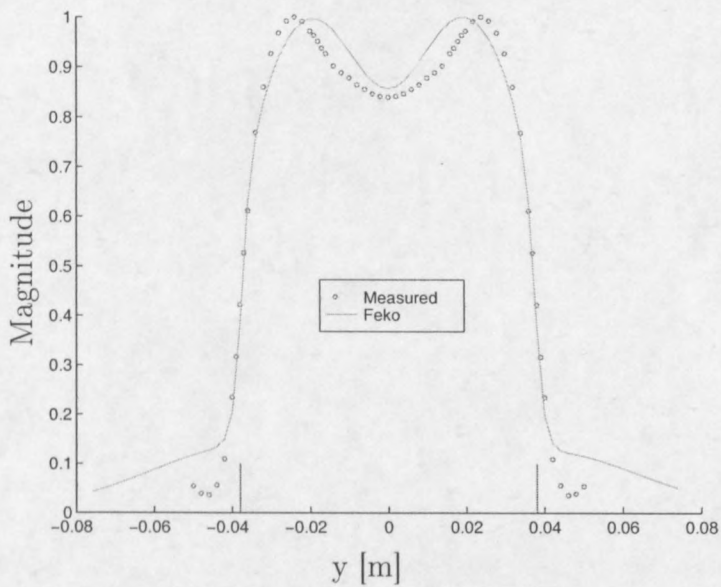


Figure 7.2: Amplitude of the theoretical and measured values of the field of the Marconi pyramidal horn.

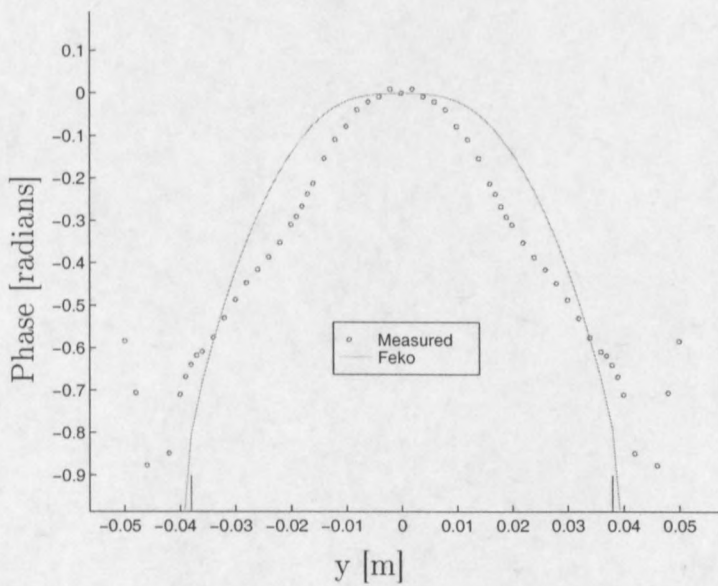


Figure 7.3: Phase of the theoretical and measured values of the field of the Marconi pyramidal horn.

Although great care was taken in the measurement of the antenna, as well as in the simulation of the theoretical data, there are differences between the measured and theoretical values. The differences are not major, but are still noticeable. Differences in the amplitude have a maximum of approximately -20 dB, which is extremely good. The maximum deviation of the phase is in the order of 10° . This corresponds very well with measurements made by other researchers [4]. Reasons for these differences can include the following:

- It is very difficult to construct a completely accurate model of the pyramidal horn antenna with respect to the feed point.
- The pyramidal horn antenna itself may differ from the perfect model used to construct the horn in the software package.
- Finite discretization can be a source of error.

The measurements shown in figures 7.2 and 7.3, were made by measuring only the one side of the antenna, and mirroring the data. The measurement would thus represent an ideal symmetric antenna. Measurements of both sides of the symmetry axis was also made. These can be seen in figures 7.4, 7.5 and 7.6.

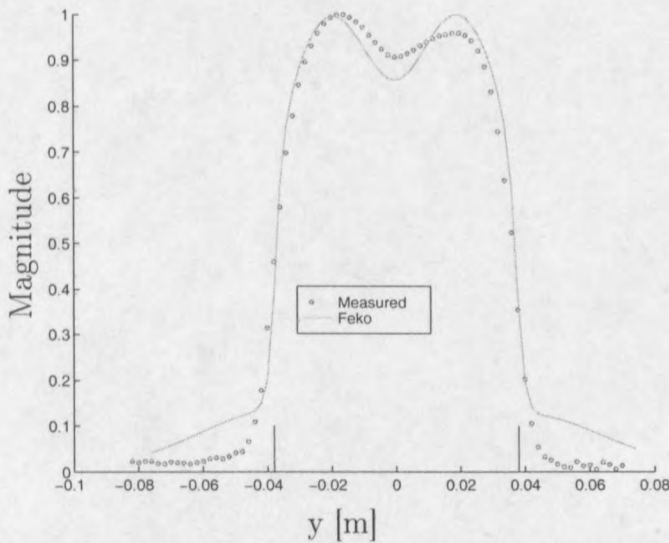


Figure 7.4: Amplitude of the theoretical and measured values of the field of the Marconi pyramidal horn: complete measurement.

It was first thought that the unsymmetric form of the near field was caused by unwanted reflections near the antenna, even though the ground was covered

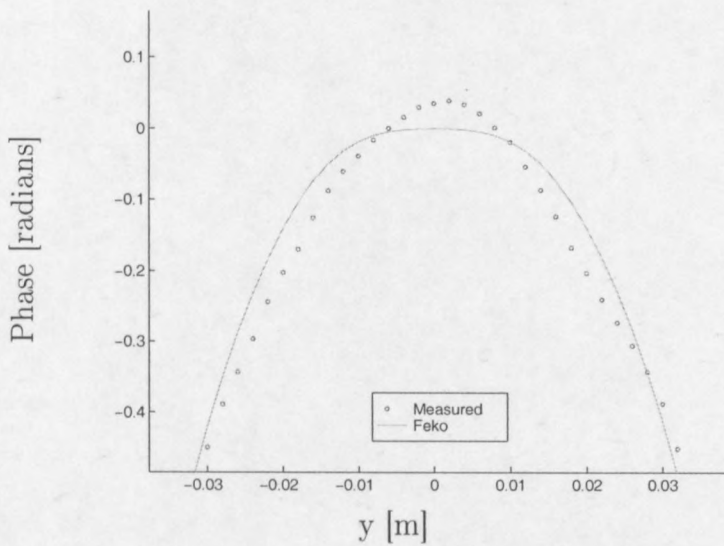


Figure 7.5: Phase of the theoretical and measured values of the field of the Marconi pyramidal horn: complete measurement; zoomed data.

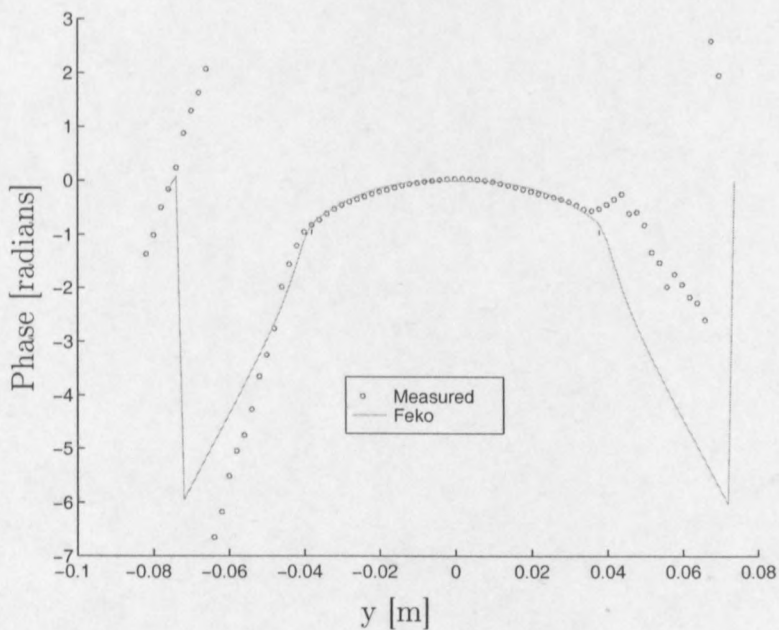


Figure 7.6: Phase of the theoretical and measured values of the field of the Marconi pyramidal horn: complete measurement.

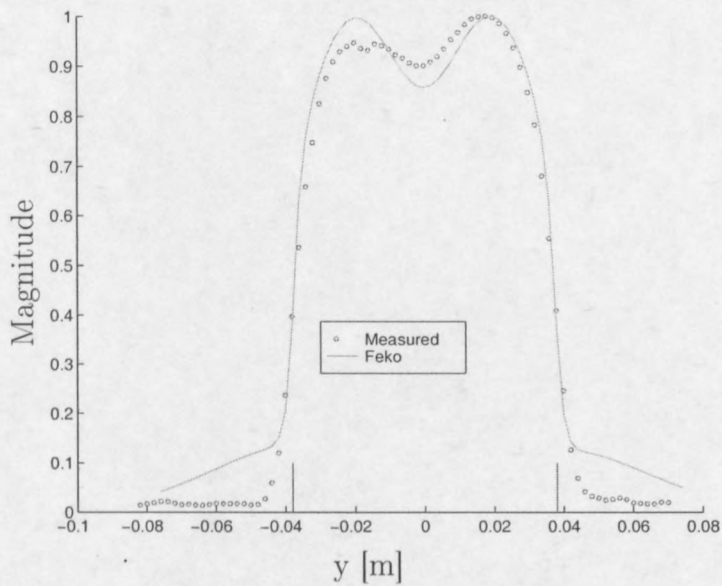


Figure 7.7: Amplitude of the theoretical and measured values of the field of the Marconi pyramidal horn: complete measurement with horn rotated 180° .

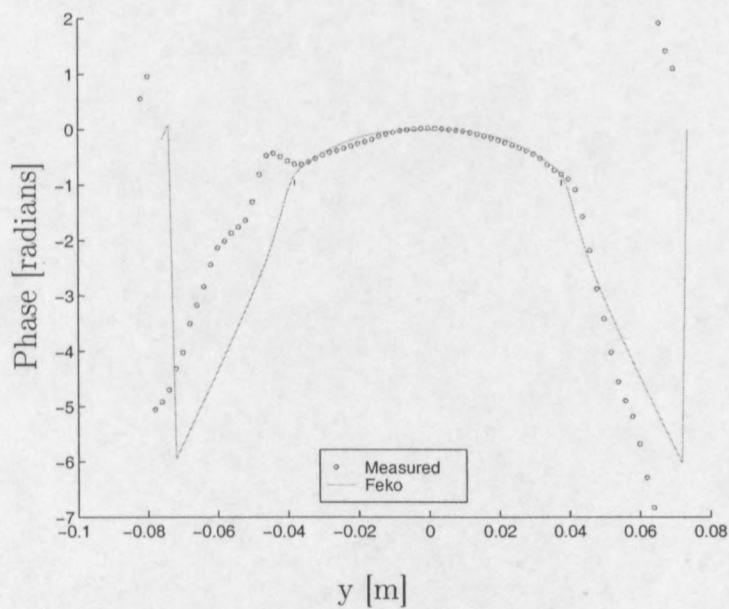


Figure 7.8: Phase of the theoretical and measured values of the field of the Marconi pyramidal horn: complete measurement with horn rotated.

with absorbing material. The horn antenna was then rotated by an angle of 180° , and the entire measurement was repeated. If the same shape were to be found as in the first measurement, there would be a measurement error, and the setup would have to be recounted for. However, the measurements were found to be as in figure 7.7 and 7.8.

From figures 7.4 and 7.7, it is very clear that it was not the measurement setup that caused a measurement error. Except for two odd points in figure 7.7—which are definite measurement errors with unknown origin—the two measurements are exact mirror images of each other. It is therefore easy to see that the measurements are the true fields of the antenna. This is also a very good demonstration of the repeatability of the system.

As far as the amplitudes are concerned, there is quite good agreement between the measured and the theoretical data. The phase, however, had to be corrected in the diffraction region. The reason for this is the way in which the phase is computed. The phase was shifted by an amount equal to $n\pi$ to fit on the theoretical curves.

7.2 E-Plane Sectoral Horn

An E-plane sectoral horn was designed and built. The built antenna's geometry was measured to compare it with the designed data (figure 7.9).

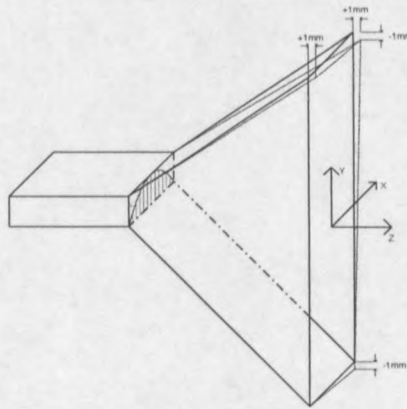


Figure 7.9: An E-plane sectoral horn. The solid lines represent the designed antenna, while the broken lines represent the built antenna. Note the differences.

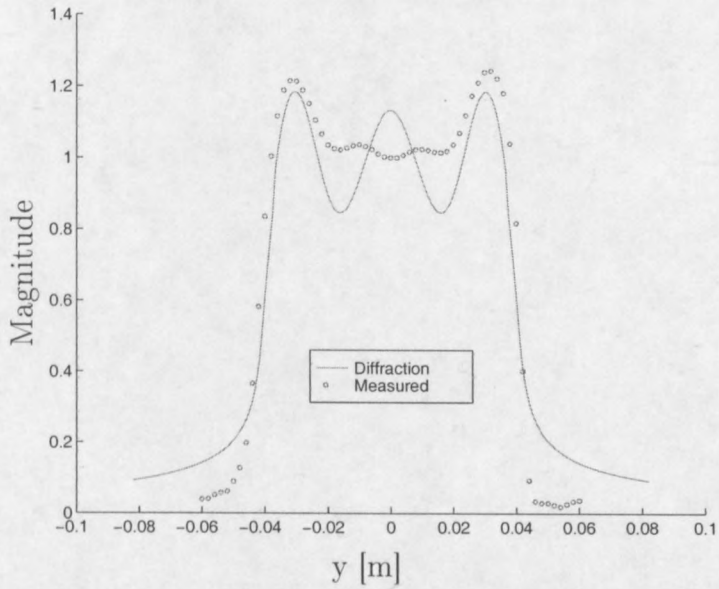


Figure 7.10: Amplitude of the theoretical and measured values of the field of the custom built E-plane horn.

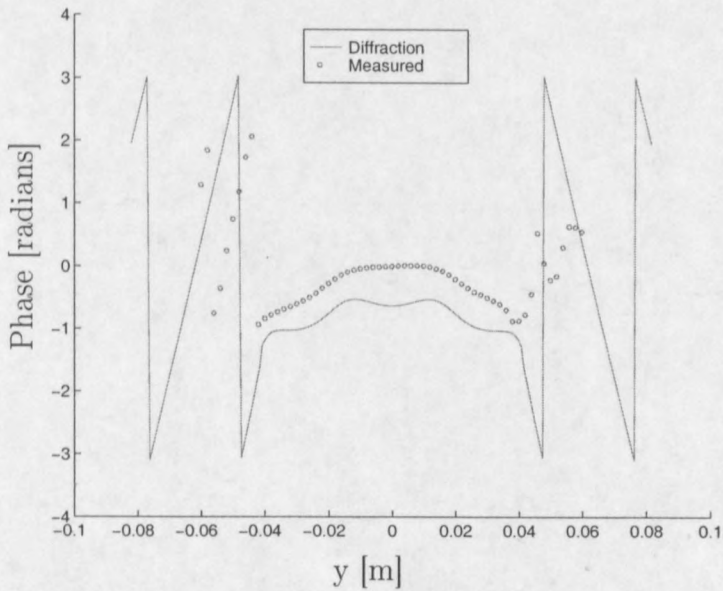


Figure 7.11: Phase of the theoretical and measured values of the field of the E-plane horn.

The measurements were made along the y -axis with $x = 0$ and $z = 2$ mm. Because of the asymmetry of the antenna, it would be expected that the measured field be asymmetric as well. This can be seen in figures 7.10 and 7.11. On the positive y -axis, the fields are a bit larger and there is a slight deviation from symmetry in the phase. The correlation between the measured and simulated results are reasonably good for the magnitude. There is much more deviation in the phase. This deviation is most likely because of errors in the manufacturing of the antenna. Because the sides of the horn were not sealed everywhere, leaking fields could cause the phase to be altered.

7.3 A Simple Waveguide

It was decided that a very simple structure, with a very simple theoretical model, should be measured. The simple structure would allow for easy simulation in a software package. The measurements were again made on the y -axis at $x = 0$ and with $z = 1$ cm. The orientation of the axis can be seen in figure 7.12.

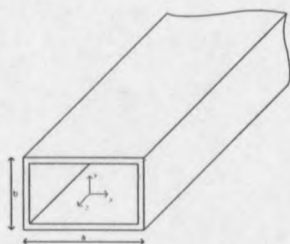


Figure 7.12: A simple waveguide.

Prior to these measurements, the laser diode was damaged. This inhibited the modulation effect, which caused the system to lose much of its sensitivity. Although the probe was modulated by a very faint laser, it was not modulated strongly enough. It is clear that the amplitude measurements correlate well in front of the mouth of the waveguide, where there is a strong field to be scattered. However, measurements of the much weaker diffraction fields in the shadow region of the waveguide are shattered by noise and insensitivity. This is also clear in the phase measurement in figure 7.14.

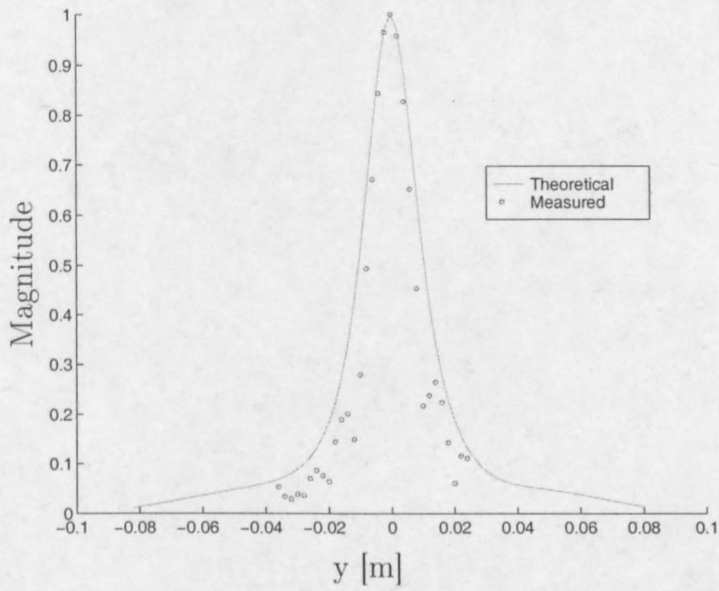


Figure 7.13: Amplitude of the theoretical and measured values of the field of an X-band waveguide.

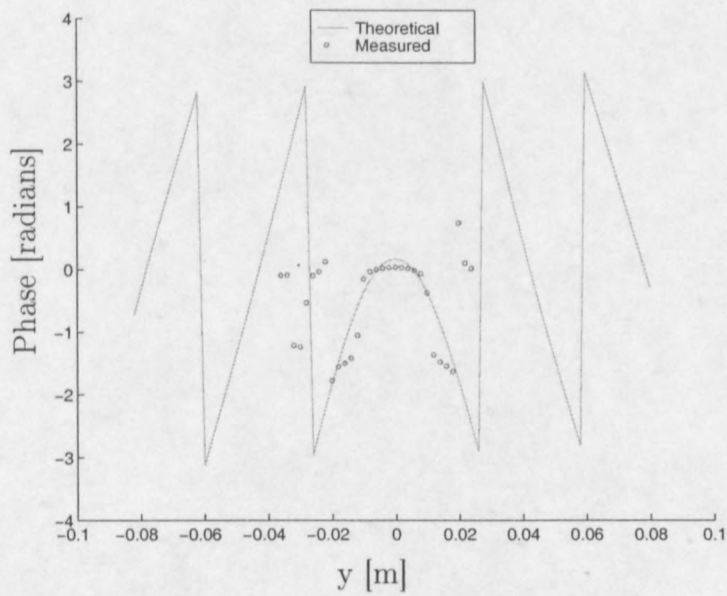


Figure 7.14: Phase of the theoretical and measured values of the field of an X-band waveguide.

7.4 Diffraction by a Half Plane

Diffraction by a half plane is easily computed by standard diffraction equations. The measurements were taken by placing the pyramidal horn antenna 150 mm from the half plane and measuring at a distance of 100 mm from the plane on the other side. The diffraction point was taken at $y = 0$. A dipole with a length of 15 mm was used to gain resonance, thus enhancing the scattered field. These measurements were made before the laser was damaged.

In the first set of measurements (figures 7.15 and 7.16), no absorbing material was placed on the ground. It was therefore expected that the reflections from the ground would have an influence on the diffraction field measurements. The effects of a standing wave should be seen.

In the second set of measurements (figures 7.17 and 7.18), absorbing material was placed on the ground. This should thoroughly suppress the reflections from the ground, and it was expected that the ripple seen in the first set of measurements would vanish.

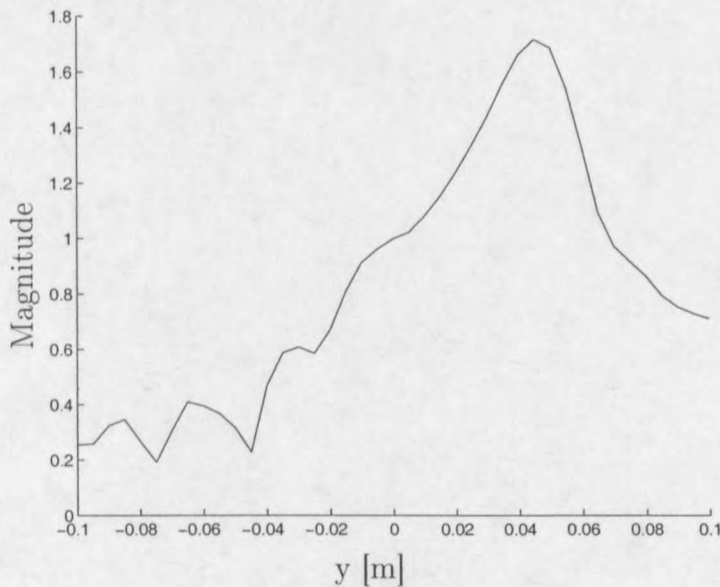


Figure 7.15: Measured diffraction by a half plane. Amplitude of the electric field with no absorbing material on the ground. $y > 0$ is in the lit region.

This effect of the reflecting fields are clear in the figures. In the second set of figures (7.17 and 7.18), the field on the positive y -axis was measured with

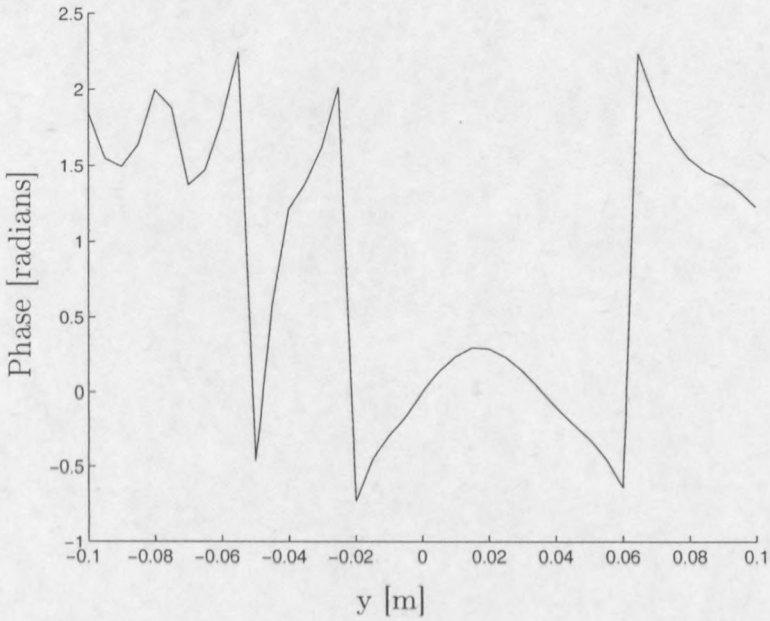


Figure 7.16: Measured diffraction by a half plane. Phase of the electric field with no absorbing material on the ground. $y > 0$ is in the lit region.

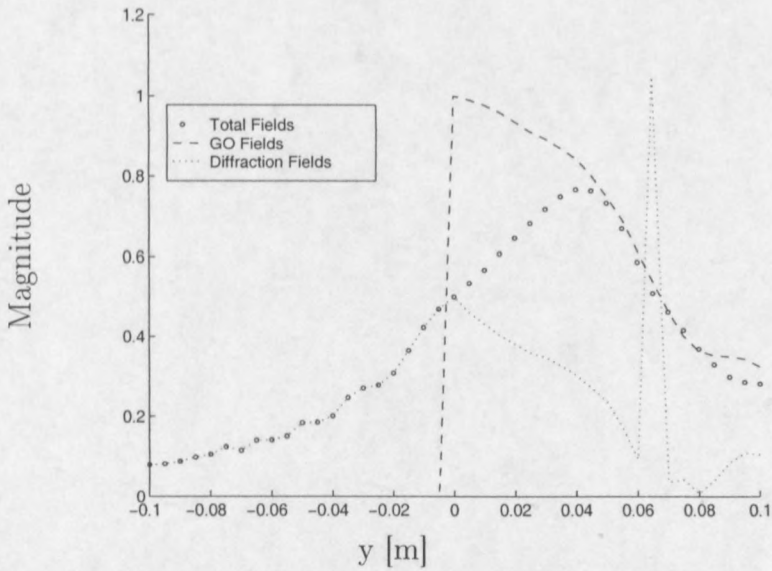


Figure 7.17: Measured and computed diffraction by a half plane. Amplitude of the electric field with absorbing material on the ground.

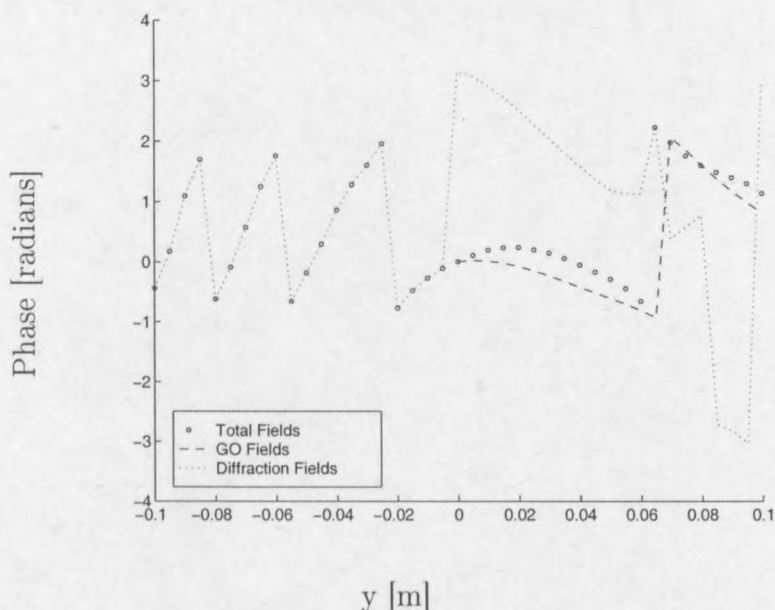


Figure 7.18: Measured and computed diffraction by a half plane. Phase of the electric field with absorbing material on the ground.

and without the presence of the half plane. These measurements would thus give the geometrical optic field as well as the diffracted fields. By subtracting the geometrical optic field from the field measured in the presence of the half plane, the diffraction fields would be obtained. This can be seen in these figures. The one odd point, which causes the sharp discontinuity, results from the discontinuity in the measured phase due to modulo 2π ambiguity.

The difference the reflections cause is also very clear in the phase plot. In figure 7.16, with no absorbing material on the ground, the phase almost has a cosine form. In figure 7.18, with the absorbing material on the ground, the phase is much more linear.

To compare the measured data with the theory, a combination of FEKO and diffraction theory was used. First, FEKO was used to compute the field at the point of diffraction in the absence of the half plane. Secondly, the field computed was used in the diffraction theory to compute the diffraction fields. FEKO was again used to compute for the fields at the observation points, should the plane be absent. In effect, the geometrical optic field was computed for the positive y -axis. Adding the calculated diffraction fields to the fields calculated with FEKO, the total fields at the observation points

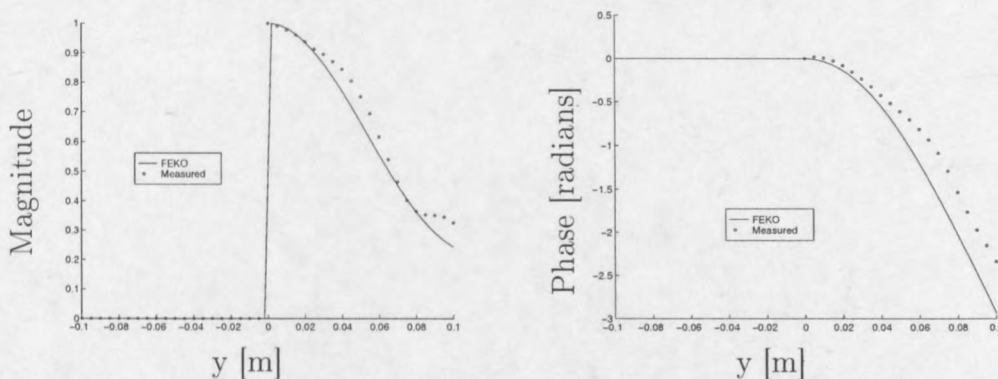


Figure 7.19: Diffraction by a half plane. The theoretical and measured geometrical optic field.

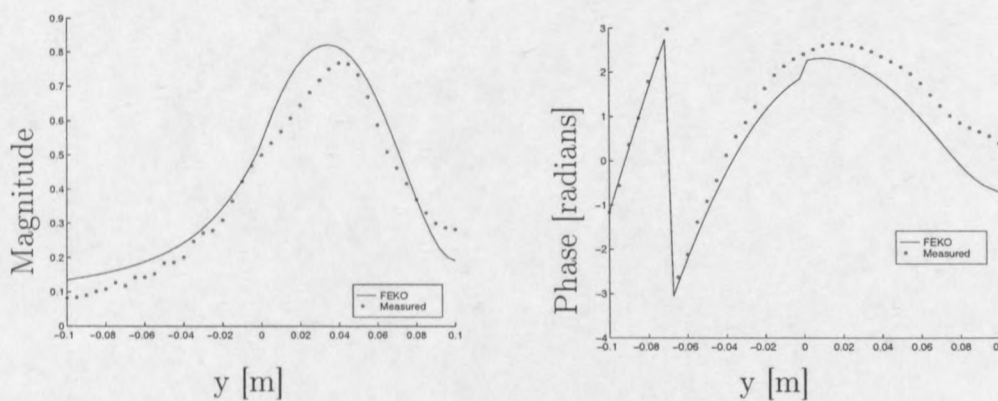


Figure 7.20: Diffraction by a half plane. The theoretical and measured field.

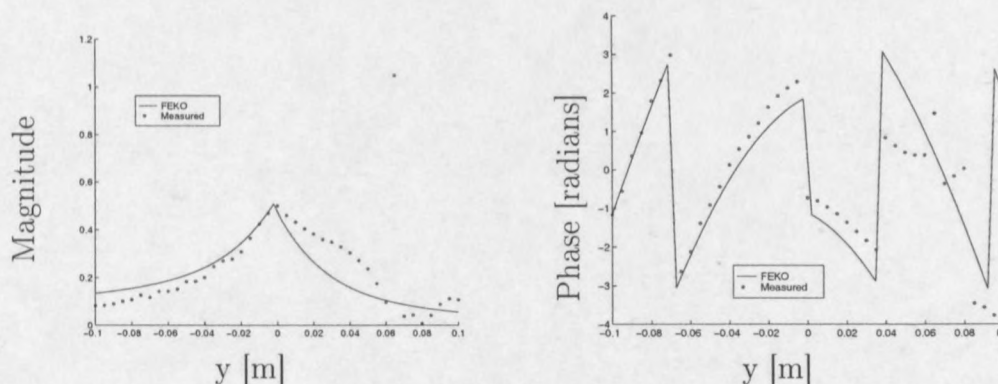


Figure 7.21: Diffraction by a half plane. The theoretical and measured diffraction field.

were obtained.

The model for the computation of the fields and the measurements made, could differ. For example, if the distance from the horn to the plane, or from the plane to the horn, differs with 1 mm only, it contributes a phase error of 12° . Because the plane was not absolutely rigid, there could exist a measurement error. Keeping this in mind, the correlation between the theoretical and measured values are very good indeed. The geometrical optic field calculated and measured differs a bit, which would add to the error of the diffraction field measurement. Despite the differences, the correlation is good. The only bad correlation is between the measured and theoretical diffraction fields for the positive y-axis in figure 7.21. The diffraction fields measured were calculated from the measured geometrical optic field and the measured total field. The errors will thus accumulate. It is therefore expected that the error will be greater.

Chapter 8

Conclusion

The field measurements made at 10 GHz with the system are in good agreement with the theoretically predicted amplitude and phase distributions. The method for measuring fields is not complicated, and the post processing of the data is neither time consuming nor difficult.

The placement of the probe is done manually, although mechanical means are used to keep the probe rigid and in the same orientation on a straight axis. This manual method is time consuming. The method should therefore be automatized, to get rid of human positioning errors and to save time.

The data acquisition technique used is also not up to standard. If the placement is automatized, the measurements should be controlled automatically by a data acquisition computer.

Despite these drawbacks, the method proved to be successful in the measurement of fields as small as -50 dBm. While the phase lacks some accuracy, the amplitude measurements are good. By concentrating on the modulation of the probe, the phase errors could be minimized.

The dynamic range of the system was found to be approximately 100 dB. The system is also linear to an error of less than 1.2% over the entire dynamic range measured. According to the measurements presented, the system could be used with confidence.

Although experiments have not been done on different frequencies, the technique is not limited to the X-band. It is possible to measure much lower and higher frequencies. The probe and the mixers are the only two components that need to be changed to change the frequency range. The higher the frequency, the smaller the probe should be made so that a high resolution and

a minimum of perturbation is maintained.

The calibration possibilities of the system is very good. Once the system is calibrated with a specific probe, the calibration constant can be used to measure any field.

Finally, it is found that the optically modulated scatterer technique offers practical prospects for quick, easy, and accurate measurements of radio frequency and microwave frequency electric fields.

Appendix A

Component Listing

See table A.1 for a list of all the components used.

Table A.1: List of Components

Description	Model	Serial No.	Manufacturer/Provider
Mixers	M14A 9745		RF-Design
Hybrid Coupler	1H0568-3		Anaren
Directional Coupler	X752A	0137	Hewlett-Packard
Synthesized Sweeper	8341B		Hewlett-Packard
Optic Cable	1mm Plastic		
Phototransistor	OP500		Optek Tech
Laser	Laser Pointer		Metrologic
Laser Module 1 mW, 670 nm, 3 V	LE07		Yebo Electronics

Appendix B

Photos

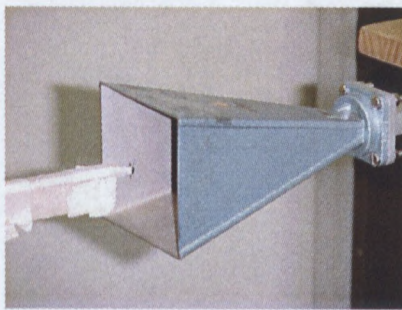


Figure B.1: Pyramidal horn antenna with probe.

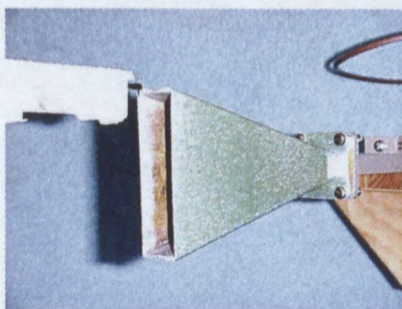


Figure B.2: The E-plane horn and probe.



Figure B.3: Busy with a setup.

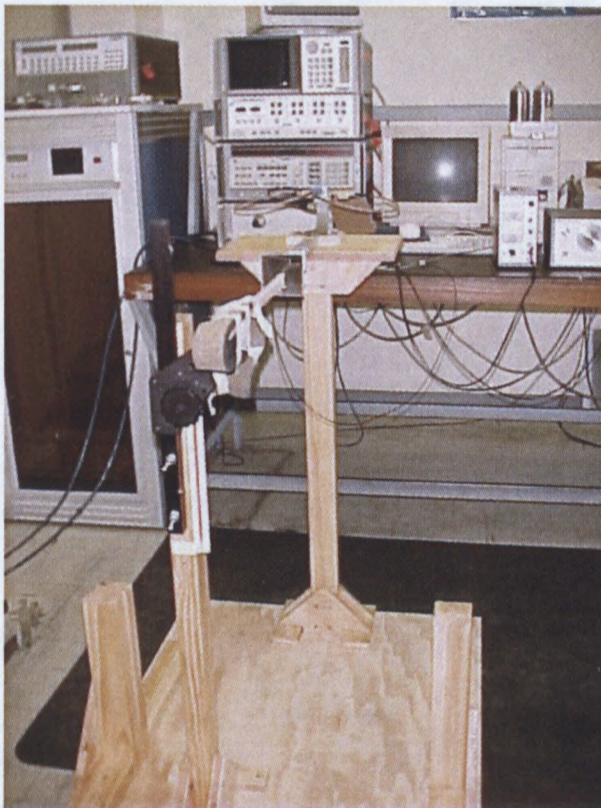


Figure B.4: The complete setup.

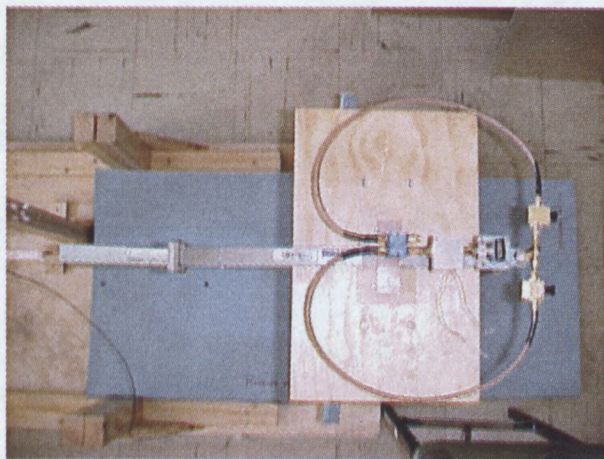


Figure B.5: Electronics as seen from the top.

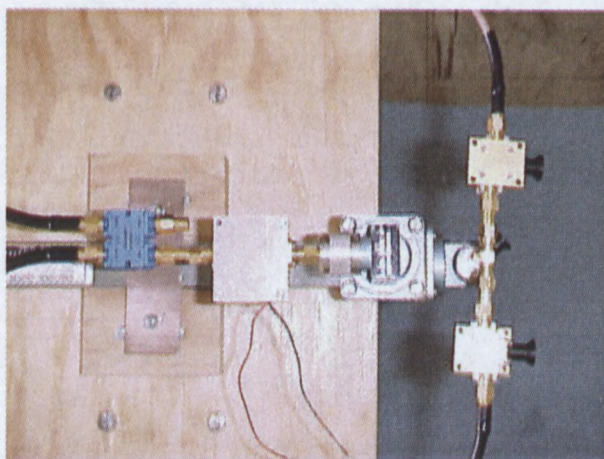


Figure B.6: IQ-detector

Appendix C

Uniform Theory of Diffraction

To analyze an antenna in terms of diffraction, it is necessary to look at all possible diffraction planes. This includes principle as well as non-principle planes. The aim here is not to give an extensive analysis of diffraction theory, nor will the equations be derived. The basic equations used will be listed, and its functions made clear.

The theory used is the Uniform Theory of Diffraction (UTD). This is an extension of the Geometrical Theory of Diffraction (GTD). GTD becomes singular in the transition region surrounding the shadow boundaries, while UTD overcomes this shortcoming. UTD is valid everywhere in space [29].

C.1 Elementary Theory

Usually, the two faces of a wedge is called the o-face and the n-face. The designation of the faces is arbitrary, but it is custom practice to measure ϕ and ϕ' from the o-face. Figure C.1 shows the different planes and boundaries. In this figure, the interior angle of the wedge is given by α , which is related to n by [29]

$$n = \frac{2\pi - \alpha}{\pi} \quad (\text{C.1})$$

For the equations that will be considered, it was assumed that the interior angle of the wedge was smaller than or equal to 180° . In other words, $1 \leq n \leq 2$. The incident shadow boundary (ISB) is the boundary for the geometrical optic field. The reflection shadow boundary (RSB) is shown as well.

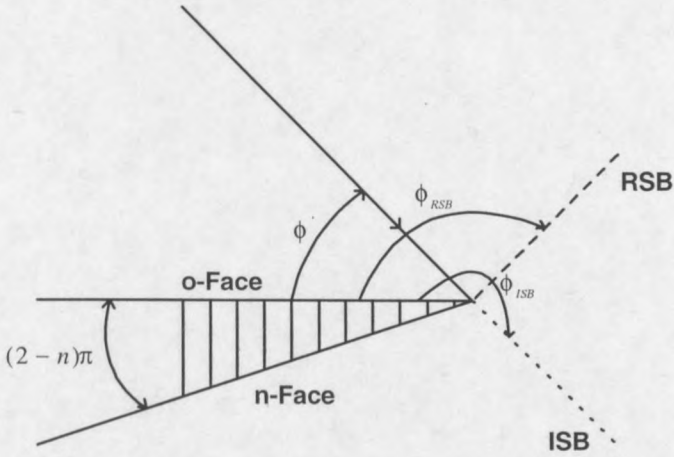


Figure C.1: Different planes and boundaries of a wedge.

In general, the following two conditions should hold true:

$$0 \leq \phi' \leq n\pi \quad (\text{C.2})$$

$$0 \leq \phi \leq n\pi \quad (\text{C.3})$$

If these equations does not hold, it is necessary to add or subtract 2π from the angle.

Figure C.2 shows the diffraction of a ray in a non-principle plane. The angle β'_0 gives the angle of deviation from the principle plane. Figure C.3 is the same as figure C.2, but viewed from the top. In this figure, the angles ϕ and ϕ' are shown as the angles to the observation and source points respectively, with reference to the o-face of the wedge.

The parameter s' is the distance between the source and the diffraction point (Q_D), with \hat{s}' as its vector. The distance from the diffraction point to the observation point is taken as s with \hat{s} as its vector (figure C.2). From the top view (figure C.3), $\rho' = s' \sin(\beta'_0)$ and $\rho = s \sin(\beta_0)$.

The two edges shown in figure C.3 can be curved so that the radius of curvature at the o-face is equal to a_0 , and that of the n-face is a_n [29]. The angles α , ϕ and ϕ' are then measured with respect to the tangential line to the surface at the diffraction point. Curvature will not be used here, and will be left out of the equations. Details on curvature can be found in [29, 30].

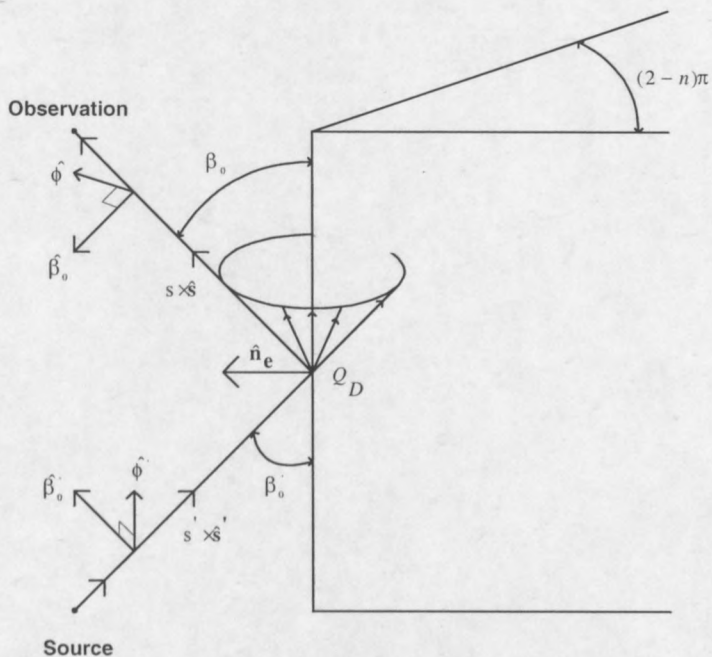


Figure C.2: Diffraction in the non-principle plane [14].

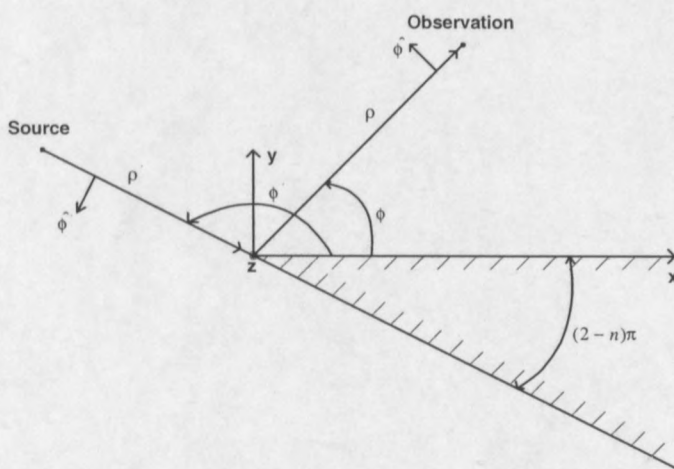


Figure C.3: Diffraction in the non-principle plane – top view [14].

C.2 Equations of the UTD

The two-dimensional edge diffracted fields are given by [14, 29]

$$E_{\beta_0}^d(s) = E_{\beta_0'}^i(Q_D) D_s A(s', s) e^{-j\beta s} \quad (\text{C.4})$$

$$E_{\phi}^d(s) = E_{\phi'}^i(Q_D) D_h A(s', s) e^{-j\beta s} \quad (\text{C.5})$$

with Q_D the diffraction point on the edge. D_s is called the soft diffraction coefficient and D_h is called the hard diffraction coefficient. $E_{\beta_0'}^i(Q_D)$ is the component of the incident E-field parallel to the plane of incidence at the point of diffraction, while $E_{\phi'}^i(Q_D)$ is the component of the incident E-field perpendicular to the plane of incidence at the point of diffraction.

The two-dimensional UTD edge diffraction coefficients are given by [14, 29]

$$D_s(L^i, L^{ro}, L^{rn}, \phi, \phi', n, \beta_0') = D_1 + D_2 - (D_3 + D_4) \quad (\text{C.6})$$

$$D_h(L^i, L^{ro}, L^{rn}, \phi, \phi', n, \beta_0') = D_1 + D_2 + (D_3 + D_4) \quad (\text{C.7})$$

The components of the diffraction coefficients are given by

$$D1 = \frac{-e^{-j\pi/4}}{2n\sqrt{2\pi\beta}\sin(\beta_0')} \cot\left[\frac{\pi + (\phi - \phi')}{2n}\right] F[\beta L^i g^+(\phi - \phi')] \quad (\text{C.8})$$

$$D2 = \frac{-e^{-j\pi/4}}{2n\sqrt{2\pi\beta}\sin(\beta_0')} \cot\left[\frac{\pi - (\phi - \phi')}{2n}\right] F[\beta L^i g^-(\phi - \phi')] \quad (\text{C.9})$$

$$D3 = \frac{-e^{-j\pi/4}}{2n\sqrt{2\pi\beta}\sin(\beta_0')} \cot\left[\frac{\pi + (\phi + \phi')}{2n}\right] F[\beta L^{rn} g^+(\phi + \phi')] \quad (\text{C.10})$$

$$D4 = \frac{-e^{-j\pi/4}}{2n\sqrt{2\pi\beta}\sin(\beta_0')} \cot\left[\frac{\pi - (\phi + \phi')}{2n}\right] F[\beta L^{ro} g^-(\phi + \phi')] \quad (\text{C.11})$$

where L^i , L^{ro} and L^{rn} are distance parameters and F is the Fresnel integral. A MATLAB program to compute this integral is included in section F.3.1. The function used by the Fresnel integral, g^\pm , is defined as follows [29]

$$g^\pm(\xi^\pm) = 2 \cos^2\left(\frac{2n\pi N^\pm - \xi^\pm}{2}\right) \quad (\text{C.12})$$

where $\xi^\pm = \phi \pm \phi'$ and N^\pm are integers nearly satisfying the following equations

$$2\pi n N^+ - (\xi^\pm) = \pi \quad (\text{C.13})$$

$$2\pi n N^- - (\xi^\pm) = -\pi \quad (\text{C.14})$$

g^+ and N^+ are associated with the n-face and g^- and N^- are associated with the o-face.

The distance parameter, L , can be simplified if it is assumed that the radius of curvature tends to infinity. This is as shown in figure C.2 and C.3. The parameters then become $L^i = L^{ro} = L^{rn} = L$ and can be expressed as [14, 31, 30]

$$L = \begin{cases} s \sin^2 \beta'_0 & \text{plane wave incidence} \\ \frac{\rho \rho'}{\rho + \rho'} & \text{cylindrical wave incidence} \\ & \rho = s \sin \beta_0, \rho' = s' \sin \beta'_0 \\ \frac{ss' \sin^2 \beta'_0}{s+s'} & \text{conical and spherical wave incidence} \end{cases} \quad (\text{C.15})$$

These equations hold for near field calculations. For calculations in the far field, equation C.15 can be simplified to

$$L = \begin{cases} s \sin^2 \beta'_0 & \text{plane wave incidence} \\ \rho' & \text{cylindrical wave incidence} \\ s' \sin^2 \beta'_0 & \text{conical and spherical wave incidence} \end{cases} \quad (\text{C.16})$$

In equations C.4 and C.5, $A(s', s)$ is the spatial attenuation factor, and is given by

$$A(s', s) = \begin{cases} \frac{1}{\sqrt{s}} & \text{plane and conical wave incidence} \\ \frac{1}{\sqrt{\rho}} & \text{cylindrical wave incidence} \\ & \rho = s \sin \beta_0 \\ \sqrt{\frac{s'}{s(s'+s)}} & \text{spherical wave incidence} \end{cases} \quad (\text{C.17})$$

for the near field calculations. For far field calculations, the attenuation factors become

$$A(s', s) = \begin{cases} \frac{1}{\sqrt{s}} & \text{plane and conical wave incidence} \\ \frac{1}{\sqrt{\rho}} & \text{cylindrical wave incidence} \\ & \rho = s \sin \beta_0 \\ \frac{\sqrt{s'}}{s} & \text{spherical wave incidence} \end{cases} \quad (\text{C.18})$$

These are the basic equations for using the uniform theory of diffraction. Details on the theory itself should be read in the textbooks, for it is impossible to repeat that theory here.

Appendix D

Theory of the E-plane Sectoral Horn

The theory of the E-plane sectoral horn will be discussed. The E-plane sectoral horn will be treated as a wedged plate, which is a form of a radial waveguide [14]. This will give an approximation to the fields in the horn antenna. Diffraction theory from appendix C will then be used to give a second order approximation to the fields in and around the sectoral horn.

D.1 Computing the Fundamental Wave

Figure D.1 shows the wedged plate which is used to compute the primary wave in the E-plane sectoral horn. The cylindrical coordinate system is used for the analysis.

The solutions of the potential function can be found in [14]. For the wedged plate of figure D.1, the solution of the potential function is given as

$$F_z(\rho, \phi, z) = \begin{bmatrix} C_1 H_m^{(1)}(\beta_\rho \rho) + D_1 H_m^{(2)}(\beta_\rho \rho) \\ C_2 \cos(m\phi) + D_2 \sin(m\phi) \\ C_3 \cos(\beta_z z) + D_3 \sin(\beta_z z) \end{bmatrix}. \quad (\text{D.1})$$

The solution to the potential function is chosen to satisfy the following conditions:

- In the ρ -direction, a traveling wave exists
- In the ϕ -direction, a periodic wave exists

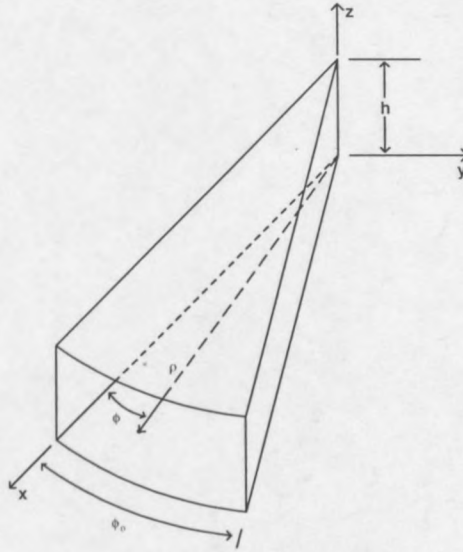


Figure D.1: Wedged plate configuration to compute the primary wave in an E-plane sectoral horn antenna.

- In the z -direction, a standing wave exists

In this equation, the following condition holds true

$$\beta_\rho^2 + \beta_z^2 = \beta^2 \quad (\text{D.2})$$

and β is defined as

$$\beta = \omega \sqrt{\mu_0 \epsilon_0} \quad (\text{D.3})$$

To solve for the potential function, the boundary conditions are set up. This will be done by setting the electric field parallel to the walls of the wedge equal to zero. From figure D.1, it is easy to see that there are two sets of fields available that are independent of each other. The first set is the fields in the ρ -direction. Therefore, setting the E_ρ -fields zero on all four planes, will satisfy the boundary conditions. The second set of fields is the fields in the ϕ -direction and the fields in the z -direction. Setting the ϕ -directed fields zero on the upper and lower planes and the z -directed fields zero on the side planes will satisfy the boundary conditions. In mathematical terms, it can be expressed as follows, for the first set of fields

APPENDIX D. THEORY OF THE E-PLANE SECTORAL HORN 77

$$\begin{aligned} E_\rho(0 \leq \rho \leq \infty, 0 \leq \phi \leq \phi_0, z = 0) &= \\ E_\rho(0 \leq \rho \leq \infty, 0 \leq \phi \leq \phi_0, z = h) &= 0 \end{aligned}$$

$$\text{and} \tag{D.4}$$

$$\begin{aligned} E_\rho(0 \leq \rho \leq \infty, \phi = 0, 0 \leq z \leq h) &= \\ E_\rho(0 \leq \rho \leq \infty, \phi = \phi_0, 0 \leq z \leq h) &= 0 \end{aligned}$$

and for the second set of fields

$$\begin{aligned} E_\phi(0 \leq \rho \leq \infty, 0 \leq \phi \leq \phi_0, z = 0) &= \\ E_\phi(0 \leq \rho \leq \infty, 0 \leq \phi \leq \phi_0, z = h) &= 0 \end{aligned}$$

$$\text{and} \tag{D.5}$$

$$\begin{aligned} E_z(0 \leq \rho \leq \infty, \phi = 0, 0 \leq z \leq h) &= \\ E_z(0 \leq \rho \leq \infty, \phi = \phi_0, 0 \leq z \leq h) &= 0 \end{aligned}$$

For TE_z -propagation, the following equations should be satisfied

$$\begin{aligned} E_\rho &= -\frac{1}{\epsilon \rho} \frac{\partial F_z}{\partial \phi} \\ E_\phi &= \frac{1}{\epsilon} \frac{\partial F_z}{\partial \rho} \\ E_z &= 0 \end{aligned} \tag{D.6}$$

where F_z must satisfy the scalar wave equation

$$\nabla^2 F_z(\rho, \phi, z) + \beta^2 F_z(\rho, \phi, z) = 0 \tag{D.7}$$

To simplify the analysis, it is assumed that the reflections inside the horn are negligible. For this reason, only the forward wave will be recognized and the backward wave will be ignored. For ρ^+ -travel, $H_m^{(1)} = 0$.

To solve for the unknowns in equation D.1, the boundary condition in equation D.4 will be used. If the boundary condition of equation D.5 is used, the solution for E_z will be trivial. Solving for E_ρ in equation D.6 gives

$$\begin{aligned} E_\rho &= -\frac{m}{\epsilon \rho} [C_1 H_m^{(1)}(\beta_\rho \rho) + D_1 H_m^{(2)}(\beta_\rho \rho)] \cdot \\ &\quad [-C_2 \sin(m\phi) + D_2 \cos(m\phi)] \cdot \\ &\quad [C_3 \cos(\beta_z z) + D_3 \sin(\beta_z z)] \end{aligned} \tag{D.8}$$

By using the first boundary condition for E_ρ —from equation D.4—at $z = 0$, it is easily seen from the third term in equation D.8 that $C_3 = 0$. This is derived from a substitution of $z = 0$ into equation D.8. For the upper plane at $z = h$, substitution of z into equation D.8 results in $D_3 \sin(\beta_z h) = 0$. This has the trivial solution of $D_3 = 0$. Apart from the trivial solution, the boundary condition results in

$$\beta_z = \frac{n\pi}{h} \quad \text{for } n = 1, 2, 3, \dots \quad (\text{D.9})$$

For the side walls the treatment is exactly the same. Setting $\phi = 0$ in equation D.8 results in $D_2 = 0$. Setting $\phi = \phi_0$, results in (apart from the trivial solution where $C_2 = 0$)

$$m = \frac{p\pi}{\phi_0} \quad \text{for } p = 1, 2, 3, \dots \quad (\text{D.10})$$

From the above equations it can be seen that $n \neq 0$. If n equals zero, the solution will again be trivial, because the fields will be zero everywhere.

Remembering that $H_m^{(1)} = 0$ for a wave traveling in the ρ^+ -direction, the solution for the E-fields inside the E-plane horn antenna is given by

$$\begin{aligned} E_\rho^+ &= A_{pn} \frac{p\pi/\phi_0}{\epsilon\rho} H_m^{(2)}(\beta_\rho\rho) \sin\left(\frac{p\pi}{\phi_0}\phi\right) \sin\left(\frac{n\pi}{h}z\right) \\ E_\phi^+ &= A_{pn} \frac{\beta_\rho}{\epsilon} H_m^{(2)'}(\beta_\rho\rho) \cos\left(\frac{p\pi}{\phi_0}\phi\right) \sin\left(\frac{n\pi}{h}z\right) \\ E_z^+ &= 0 \end{aligned} \quad (\text{D.11})$$

In equation D.11, $H_m^{(2)}$ is the Hankel function of the second kind of order m . $H_m^{(2)'}$ is the derivative of $H_m^{(2)}$ with respect to ρ .

D.2 Hankel Functions

The Hankel functions used in the derivation of the primary wave of the E-plane horn antenna can be written in terms of Bessel functions as [14, 32]

$$H_\eta^{(1)}(\chi) = J_\eta(\chi) + jY_\eta(\chi) \quad (\text{D.12})$$

$$H_\eta^{(2)}(\chi) = J_\eta(\chi) - jY_\eta(\chi) \quad (\text{D.13})$$

The derivative of the Hankel functions with respect to ρ can be computed by a combination of the Hankel functions itself, so that

$$\frac{\partial}{\partial x} [Z_\alpha(\beta x)] = -\beta Z_{\alpha+1}(\beta x) + \frac{\alpha}{x} Z_\alpha(\beta x) \quad (\text{D.14})$$

D.3 Computing the Diffraction Fields

The diffraction fields are computed using the equations listed in appendix C.2. The fields will be computed along the y-axis, as shown in figure D.2, in the plane parallel to the yz-plane at $x = 0$.

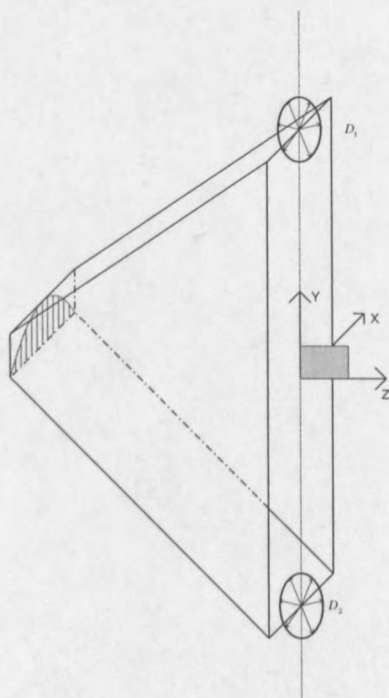


Figure D.2: Diffraction along the y-axis of the E-plane horn antenna.

In this figure, it is clear that the only two points that will contribute to the diffraction field along the y-axis, is the points at D_1 and D_2 . The fields are normally incident on these two points, therefore, the diffracted fields that will emanate from these points, will be in the yz-plane. For normal incidence

$$\beta_0 = \beta'_0 = \frac{\pi}{2} \quad (\text{D.15})$$

The diffraction fields will be computed to the second order. The first order diffraction will result from the primary wave, while the second order diffrac-

tion will result from the first order diffraction fields at the diffraction points. In mathematical terms, the total field can be written as

$$E_T(y) = E_i(y) + E_1^{D_1}(y) + E_1^{D_2}(y) + E_2^{D_1}(y) + E_2^{D_2}(y) \quad (\text{D.16})$$

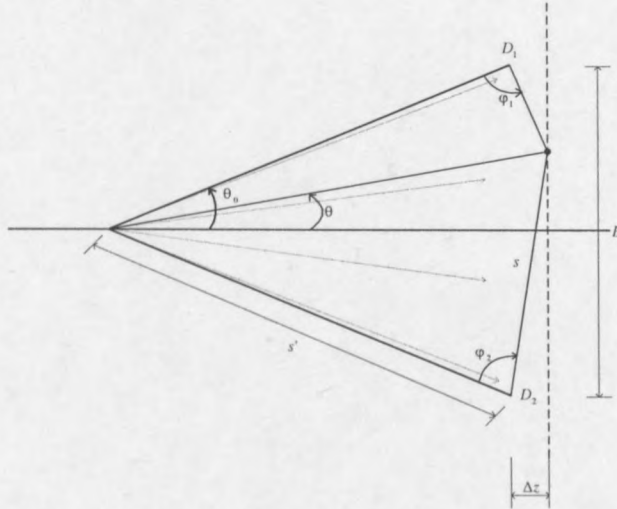


Figure D.3: Geometry of the E-plane horn antenna fields.

Figure D.3 shows the geometry of the diffraction setup. The field is calculated on the y -axis, at a distance Δz from the aperture opening. The angle from the wedge plane (the upper and lower panel of the horn antenna) to the observation point is given as φ_1 and φ_2 for the first and second diffraction points respectively. Assuming that the source of the primary wave is at the apex, the angle from the source to the observation point is given as θ , while the angle between the top and lower panels of the horn is given as $2\theta_0$. It is clear that the angle of incidence from the main source to the point of diffraction is $\varphi_0 = 0^\circ$. From equation C.1 and the geometry of the horn antenna, it is clear that $n = 2$.

To calculate the first order diffraction points, the value of the primary wave should be calculated at each of the diffraction points, according to equation C.5. The diffraction equations can now be used to calculate the diffraction fields at the observation points. To calculate the second order diffraction fields, the first order diffraction fields should be calculated at the diffraction points. The diffraction of these fields will add to the first order diffraction fields at the observation points.

D.3.1 First Order Diffraction Fields

Instead of doing an axial transformation on the equations of equation D.11, the coordinate system is preserved and the fields calculated for the specific system. The calculated fields are then transformed into the required system.

According to equation D.11, there is only an E_ϕ field component for the TE_{z10} mode. The fields are thus perpendicular on the incident plane. For this reason, only the hard diffraction coefficients will be used from equation C.5. Because the fields are of cylindrical form, the distance parameter, L (equation C.15), and the spatial attenuation factor, A (equation C.17), for cylindrical wave incidence will be used.

From equation D.15 and C.15, it is found that $\rho' = s'$ and $\rho = s$. The length of the top and bottom panel of the horn antenna (the distance from the source to the point of diffraction) is equal to s' for both diffraction points. The distance from the diffraction points to the observation points is equal to

$$s_1 = \sqrt{\text{abs}\left(\frac{B}{2} - y\right)^2 + \Delta z^2} \quad (\text{D.17})$$

$$s_2 = \sqrt{\text{abs}\left(-\frac{B}{2} - y\right)^2 + \Delta z^2} \quad (\text{D.18})$$

The angle φ_0 is equal to zero. The angles φ_1 and φ_2 are calculated with the aid of the geometrical analysis as was done in figure D.4 for the angle φ_1 . The equations for the calculation of the angles are

$$\varphi_1 = \begin{cases} \frac{\pi}{2} - \theta_0 + \arctan\left(\frac{\Delta z}{B/2 - y}\right) & \text{for } y \leq B/2 \\ \frac{3\pi}{2} - \theta_0 - \arctan\left(\frac{\Delta z}{y - B/2}\right) & \text{for } y > B/2 \end{cases} \quad (\text{D.19})$$

and

$$\varphi_2 = \begin{cases} \frac{3\pi}{2} - \theta_0 - \arctan\left(\frac{\Delta z}{y + B/2}\right) & \text{for } y < -B/2 \\ \frac{\pi}{2} - \theta_0 + \arctan\left(\frac{\Delta z}{B/2 + y}\right) & \text{for } y \geq -B/2 \end{cases} \quad (\text{D.20})$$

The first order coefficients can now be calculated, and substituted in equation C.5 to solve for the diffraction fields at the observation points.

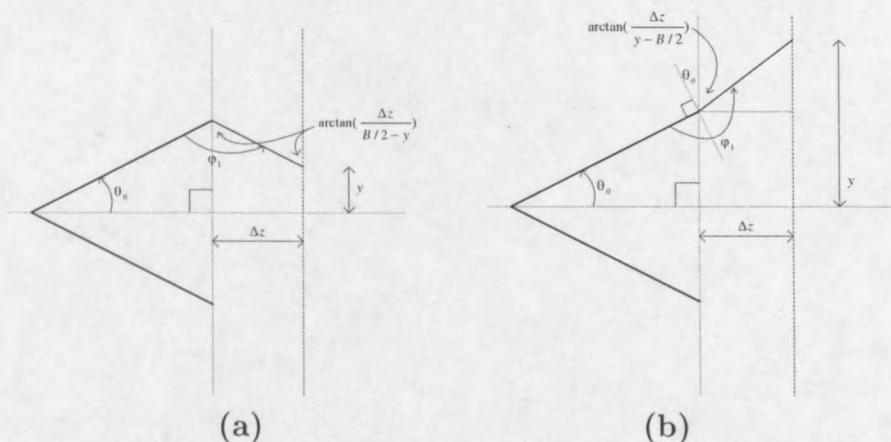


Figure D.4: Determining the angle φ_1 for (a) $y \leq \frac{B}{2}$ and (b) $y > \frac{B}{2}$.

D.3.2 Second Order Diffraction Fields

To calculate the second order diffraction fields, the first order diffraction fields should be known at the point of diffraction. The distance parameters, s_1 and s_2 , are both equal to B , the length of the aperture opening. s' is the distance from the source to the diffraction point, and is still equal to the length of the top and bottom panel of the horn. φ_0 is still equal to zero, while φ_1 and φ_2 are both equal to $\frac{\pi}{2} - \theta_0$ from equations D.19 and D.20. The diffraction coefficients can now be calculated and substituted in equation C.5 to solve for the first order diffraction fields at the diffraction points.

To calculate the second order diffraction coefficients, the parameters change to adapt to the new source positions. Instead of φ_0 being zero, it is now equal to $\frac{\pi}{2} - \theta_0$, which is clear from figure D.3. The angles φ_1 and φ_2 are the same as for the first order diffraction coefficients. The distance parameters change as well. s' , the distance from the source to the diffraction point, is now equal to the length of the aperture opening, B . The distances from the diffraction points to the observation points, s_1 and s_2 , do not change, but is equal to that of first order diffraction. The diffraction coefficients can now be calculated with the aid of equation C.7 and substituted in equation C.5 to solve for the second order diffraction fields.

It is possible to repeat the steps for a third order approximation as well as higher orders.

Appendix E

Design of the E-Plane Sectoral Horn

An E-plane horn antenna was designed using the design rules from [33, 34].

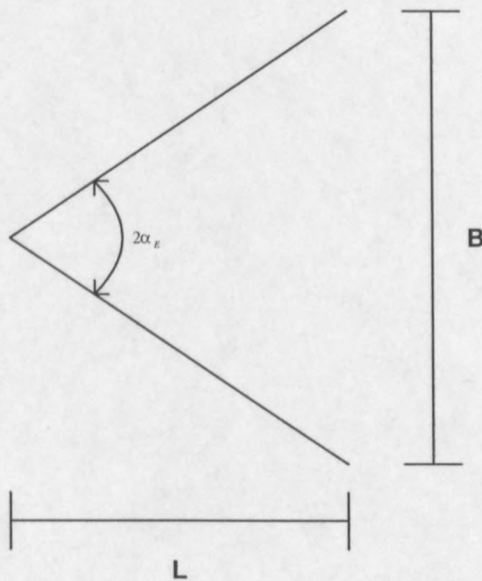


Figure E.1: Geometry of the designed E-plane horn.

The angle α_E was chosen as 15° , so that the flare angle would be 30° . The length of the aperture, B , was chosen to be 82 mm. These parameters resulted in a horn length, from the apex, to be 153 mm.

Appendix F

MATLAB Program Code

F.1 Computation of the E-field from the Measured Data

An example program is given here for a two-point measurement with an extra calibration point. Any number of points can be imported by adding extra modules.

```
%Jan Tait
%20 August 2000
%Computation of the measured data for the Optically Modulated Scatterer
%V = kE2

%Measurement without Probe - parasitic cancellation
%-----
load dsp.mat                                %Filename - 0 degree
ksp = sum(wavedata(1,:).*wavedata(2,:));    %Correllate the two channels
clear wavedata                              %Clear Memory

load jdsp                                   %90 Degree from Hybrid
jksp = sum(wavedata(1,:).*wavedata(2,:));    %Correllate two channels
clear wavedata                              %Clear Memory

%Computation of the calibration constant
%-----
load kal                                    %0 Degree
kkal = sum(wavedata(1,:).*wavedata(2,:)) - ksp;
clear wavedata

load jkal                                   %90 Degree
```

APPENDIX F. MATLAB PROGRAM CODE

85

```

jkkal = sum(wavedata(1,:).*wavedata(2,:)) - jksp;
clear wavedata

Vkal = kkal + j*jkkal           %Complex Voltage

k = Vkal/(1^2)                  %Calibration Constant

Ekal = sqrt(Vkal)/sqrt(k)      %Recomputes E-field

%Field point calculation
%-----
%First Point
%-----
load d1
k1 = sum(wavedata(1,:).*wavedata(2,:)) - ksp;
clear wavedata

load jd1 jk1 = sum(wavedata(1,:).*wavedata(2,:)) - jksp;
clear wavedata

V1 = k1 + j*jk1;
E1 = sqrt(V1)/sqrt(k)

%Second Point
%-----
load d2
k2 = sum(wavedata(1,:).*wavedata(2,:)) - ksp;
clear wavedata

load jd2
jk2 = sum(wavedata(1,:).*wavedata(2,:)) - jksp;
clear wavedata

V2 = k2 + j*jk2;
E2 = sqrt(V2)/sqrt(k)

%-----
%More Points could be added as needed...
%-----

%The Electric Field data are stored
%-----
%Place data in array
%-----
E = [E1 Ekal E2];
%Store in filename Edat.mat
%-----
save Edat.mat E

```


F.2 Hankel Functions

F.2.1 Hankel Function

The Hankel function computes the function $H_{\eta}^{(2)}(\chi)$. “alpha” is substituted for η and “x” is substituted for χ . To compute the Hankel function of the first kind, substitute the “-” for a “+” in the function.

```
function H = hankel(alpha,x);

%Jan Tait
%7 August 2000
%Hankel-function -- The Bessel functions are used to compute
%the hankel function

H = bessel(alpha,x) - j*bessely(alpha,x);
```

F.2.2 Derivative of the Hankel Function

The Hankel derivative function computes the function

$$\frac{\partial}{\partial \chi} [H_{\eta}(\beta \chi)]$$

“alpha” is substituted for η and “x” is substituted for χ . “Beta” is substituted for β . This function computes the derivative of the Hankel function of the first and second kind.

```
function Ha = hankelaf(alpha,x,Beta);

%Jan Tait
%7 Augustus 2000
%Hankel(derivative)-function -- Using the previously defined
%hankel function

Ha = -Beta.*hankel(alpha+1, Beta*x) + (alpha./x).*hankel(alpha,
Beta*x);
```

F.3 Diffraction Coefficient Computation

F.3.1 Fresnel Integral Computation

The program codes for the Fresnel integral computation were used in a course at the University of Stellenbosch and is not my own work [35]. I include it so that the programs used are complete.

Fresnel Coefficients

```
% Coefficients for Fresnel intergral approximation
% See : J Boersma, Jour. Math. Comp , Vol 14, p380, 1960
```

```
global FresCa FresCb FresCc FresCd;
```

```
FresCa = [1.595769140; -0.000001702; -6.808568854;
          -0.000576361; 6.920691902; -0.016898657;
          -3.050485660; -0.075752419; 0.850663781;
          -0.025639041; -0.150230960; 0.034404779];
```

```
FresCb = [-0.000000033; 4.255387524; -0.000092810;
          -7.780020400; -0.009520895; 5.075161298;
          -0.138341947; -1.363729124; -0.403349276;
          0.702222016; -0.216195929; 0.019547031];
```

```
FresCc = [0; -0.024933975; 0.000003936; 0.005770956;
          0.000689892; -0.009497136; 0.011948809;
          -0.006748873; 0.000246420; 0.002102967;
          -0.001217930; 0.000233939];
```

```
FresCd = [0.199471140; 0.000000023; -0.009351341;
          0.000023006; 0.004851466; 0.001903218;
          -0.017122914; 0.029064067; -0.027928955;
          0.016497308; -0.005598515; 0.000838386];
```

Fresnel Computation: 1

```
function Y = Fresnel1(x)
%
% Init Coef with FresCoef
%
global FresCa FresCb FresCc FresCd;
vecn = ones(11,1);
Int_inf = (1-i)/2;
pi2 = sqrt(pi/2);
```



```

x = x.*x;
Ex = exp(-i*x);
xt = x<4;

if any(xt),
    k = find(xt);
    z = x(k)/4;
    Y(k) = Ex(k).*sqrt(z).*[(FresCa+i*FresCb).'*[ones(1,length(z)); cumprod(vecn*z)]];
    Y(k) = pi2*(Int_inf - Y(k));
end;

xt = ~xt;

if any(xt),
    k = find(xt);
    z = (4)./x(k);
    Y(k) = -pi2*Ex(k).*sqrt(z).*[(FresCc+i*FresCd).'*[ones(1,length(z)); cumprod(vecn*z)]];
end;

```

Fresnel Computation: 2

```

function Y = Fresnel2(x)

% Init Coef with FresCoef
%

Y = 2.* j .* sqrt(x) .* exp(j.*x) .* fresnel1(sqrt(x));

```

F.3.2 Computation of the Diffraction Coefficients

```

function D = DifKcoef(L, Psi, n, Beta0, Lambda);
%Jan Tait
%This procedure computes the diffraction coefficients
%D = DifKcoef(L, Psi, n, Beta0, Lambda)
%Psi = (phi-phi') or (phi+phi')

FresCoef; %Initialize Fresnel Coefficients

Beta = 2*pi/Lambda;
Kons = -exp(-j*pi/4)/(2*n*sqrt(2*pi*Beta)*sin(Beta0));

Cotf1 = cot((pi+Psi)/(2*n));
Cotf2 = cot((pi-Psi)/(2*n));

Np = round((pi+Psi)/(2*n*pi));
Nm = round((-pi+Psi)/(2*n*pi));

```

```

gp = 1 + cos(Psi-2*n*pi*(Np));
gm = 1 + cos(Psi-2*n*pi*(Nm));

Fres1 = Fresnel2(Beta*L.*gp);
Fres2 = Fresnel2(Beta*L.*gm);

D = Kons*(Cotf1.*Fres1 + Cotf2.*Fres2);

```

F.4 E-Plane Horn Antenna Field Calculation

```

%Jan Tait
%4 October 2000
%Compute the pattern of an E-plane Horn antenna

close all
clear all

%First set up the constants
%-----
%Dimensional
%-----
Zfront = 0.002;           %Distance in front of horn
a = 22.86e-3;             %X-band Waveguide
b = 10.16e-3;
B = 82/1000;              %Horn aperture Opening
phi0 = 29.59;             %Flair angle -
phi0 = phi0*pi/180;       %in radians
rho = 0.15523;           %Horn length from apex
Rho = 0.16055;           %Sidelength of horn from apex

%Constants
%-----
n = 1;                    %From Theory
p = 0; orde = 0;
w = 2*pi*10e+9;          %Frequency
eps = 8.854e-12;
Beta = w*sqrt(4*pi*1e-7*eps); %Beta in free space
Betaz = n*pi/a;          %From theory
Betap = sqrt(Beta^2 - Betaz^2);
Apn = 1;                  %Proportional multiplier
m = p*pi/phi0;

%The Ey-components are calculated for the E-plane
%-----
%Constants
%-----
z = a/2;                  %The center of the horn

```


APPENDIX F. MATLAB PROGRAM CODE

90

```

x = rho; %At the aperture opening
Disk = 200; %Discretization number
y = -B/2: B/(Disk-1): B/2; %y-discretized

rho = sqrt(x^2 + y.^2); %Convert cartesian to
phi = atan(y/x) + phi0/2; %cylindrical coordinates

%Calculations for the primary field
%-----
Hank = hankel(orde,Betap*rho); %Compute the Hankel
Hankaf = hankelaf(orde,rho,Betap); %functions

%Compute the \rho and \phi components
Epe = Apn*m./(eps*rho) .* Hank .* sin(m*phi) .* sin(Betaz*z);
Ephie = Apn * Betap/(eps) .* Hankaf .* cos(m*phi) .* sin(Betaz*z);

%Convert the above components to Ey-components
Eye = Epe.*sin(phi-phi0/2) + Ephie.*cos(phi0/2 - phi);

%Diffraction at the different points will now be considered
%-----
%Constants needed for diffraction
%-----
Beta0 = pi/2; %Incident angle
n = 2; %Wedge angle coefficient
y = -B: 2*B/(Disk-1): B; %y-discretized
x = x + Zfront;
phi = atan(y/x) + phi0/2; %cylindrical coordinates

Lambda = 3e+8*2*pi/w; %Wavelength

%Computation
%Determine the E-field at the point of diffraction
%-----
Eveld = Ephie/max(abs(Ephie)); %Field perpendicular on edge

E1 = Eveld(size(Eveld,2)); %Symmetric -- should be
E2 = Eveld(1); %equal

%First order diffraction computation
%-----
%Compute the diffracted fields at the points of diffraction
%-----
rho1 = B;
rho2 = B;
L1 = (rho1*Rho)/(rho1+Rho);
L2 = (rho2*Rho)/(rho2+Rho);
A1 = 1/sqrt(rho1);

```

APPENDIX F. MATLAB PROGRAM CODE

91

```

A2 = 1/sqrt(rho2);
Zeta1m = pi/2 - phi0/2;
Zeta1p = pi/2 - phi0/2;
Zeta2m = pi/2 - phi0/2;
Zeta2p = pi/2 - phi0/2;

%The factor of 1/2 is needed for grazing incidence
Dh1 = (difkoeff(L1,Zeta1m,n,Beta0,Lambda) + difkoeff(L1,Zeta1p,n,Beta0,Lambda))/2;
Dh2 = (difkoeff(L2,Zeta2m,n,Beta0,Lambda) + difkoeff(L2,Zeta2p,n,Beta0,Lambda))/2;

%Field at Point 2 as a result of diffraction at point 1
Ed21 = E1 * Dh1 * A1 * exp(-j*Beta*rho1);
%Field at Point 1 as a result of diffraction at point 2
Ed12 = E2 * Dh2 * A2 * exp(-j*Beta*rho2);

%Determine zetam = phi - phi' and zetap = phi + phi'
%-----
%phi' = 0 for the source at the apex
%-----
for rep = 1: size(y,2)
    if y(rep)>B/2
        Zeta1(rep) = 3*pi/2 - phi0/2 - atan(Zfront/(y(rep) - B/2));
        Zeta2(rep) = pi/2 - phi0/2 + atan(Zfront/(B/2 + y(rep)));
    elseif y(rep)<=B/2 & y(rep)>=-B/2
        Zeta1(rep) = pi/2 - phi0/2 + atan(Zfront/(B/2 - y(rep)));
        Zeta2(rep) = pi/2 - phi0/2 + atan(Zfront/(B/2 + y(rep)));
    elseif y(rep)<-B/2
        Zeta1(rep) = pi/2 - phi0/2 + atan(Zfront/(B/2 - y(rep)));
        Zeta2(rep) = 3*pi/2 - phi0/2 - atan(Zfront/(-y(rep) - B/2));
    end
end

Zeta1m = Zeta1;
Zeta1p = Zeta1;
Zeta2m = Zeta2;
Zeta2p = Zeta2;

%Compute \rho for the two points, the distance between
%the diffraction points and the observation points
%-----
rho1 = sqrt(abs(B/2 - y).^2 + Zfront^2);
rho2 = sqrt(abs(-B/2 - y).^2 + Zfront^2);

%Distance parameters
%-----
L1 = (rho1*Rho)./(rho1+Rho);
L2 = (rho2*Rho)./(rho2+Rho);

```



```

%Spatial attenuation factors
%-----
A1 = 1./sqrt(rho1);
A2 = 1./sqrt(rho2);

%Computation of the diffraction points
%-----
%The factor of 1/2 is needed for grazing incidence
Dh1 = (difkoef(L1,Zeta1m,n,Beta0,Lambda) + difkoef(L1,Zeta1p,n,Beta0,Lambda))/2;
Dh2 = (difkoef(L2,Zeta2m,n,Beta0,Lambda) + difkoef(L2,Zeta2p,n,Beta0,Lambda))/2;

%Computation of the diffraction fields
%-----
Ed1 = E1 * Dh1 .* A1 .* exp(-j*Beta*rho1);
Ed2 = E2 * Dh2 .* A2 .* exp(-j*Beta*rho2);

%Set up different parameters for second order diffraction
%-----
Zeta1m = Zeta1m - (pi/2 - phi0/2);
Zeta1p = Zeta1p + (pi/2 - phi0/2);
Zeta2m = Zeta2m - (pi/2 - phi0/2);
Zeta2p = Zeta2p + (pi/2 - phi0/2);
Rho1 = B;
Rho2 = B;
L1 = (rho1*Rho1)./(rho1+Rho1);
L2 = (rho2*Rho2)./(rho2+Rho2);

%Compute second order diffracted fields
%-----
D2h1 = difkoef(L1,Zeta1m,n,Beta0,Lambda) + difkoef(L1,Zeta1p,n,Beta0,Lambda);
D2h2 = difkoef(L2,Zeta2m,n,Beta0,Lambda) + difkoef(L2,Zeta2p,n,Beta0,Lambda);

%Second order diffracted field at point 1
E2d1 = Ed12 * D2h1 .* A1 .* exp(-j*Beta*rho1);
%Second order diffracted field at point 2
E2d2 = Ed21 * D2h2 .* A2 .* exp(-j*Beta*rho2);

%Computation of the G0-field
%-----
for rep = 1: size(y,2)
    Eveld(rep) = 0;
    Ep(rep) = 0;
    if phi(rep)>=0 & phi(rep)<=phi0
        rho = sqrt(x^2 + y(rep)^2);
        Hank = hankel(orde,Betap*rho);
        Hankaf = hankelaf(orde,rho,Betap);
        Epe = Apn*m/(eps*rho) * Hank * sin(m*phi(rep)) * sin(Betaz*z);
    end
end

```

```
Ephie = Apn * Betap/(eps) * Hankaf * cos(m*phi(rep)) * sin(Betaz*z);
Eye = Epe*sin(phi(rep)-phi0/2) + Ephie*cos(phi0/2 - phi(rep));
Eveld(rep) = Eye;
Ep(rep) = Ephie;
end
end

Edt = Ed1 + Ed2;
Edt2 = E2d1 + E2d2;
Edt = Edt.*cos(phi0/2 - phi);
Edt2 = Edt2.*cos(phi0/2 - phi);
Eveld = Eveld/max(abs(Eveld));

figure
hold
plot(y, abs(Edt), 'b')
plot(y, abs(Edt2), 'm')

figure
hold
plot(y, abs(Eveld), 'b')
plot(y, abs(Eveld + Edt + Edt2), 'm')
title('ABS(Ey)')

figure
plot(y, angle(Eveld + Edt + Edt2), 'm')
```


Appendix G

FEKO Program Code

G.1 Marconi Pyramidal Horn

The model for the Marconi horn originated from [36], but was modified to suit the specific needs of the problem.

```
** A pyramidal horn for 10 GHz

#MAXLAB=20
#topfrq=10.0e9
#toplam=3E8/#topfrq    ** m!!
#segl=#toplam/8
#tril=#toplam/7

** Waveguide dimensions
#xbw=0.02286
#xbh=0.01016

** Horn dimensions
#hap=0.0755
#hlen=0.138

** Feed offset
#feedoff=-0.0256

IP                0.0001    #tril    #segl

** Define the corner points for a quarter of the horn in the
quadrants y>0 and z>0 with the feed.
** LA      2
```

```

** Wave guide end
DP   C           -0.032   #xbw/2   #xbh/2
DP   CZ          -0.032   0.0       #xbh/2
DP   CY          -0.032   #xbw/2   0.0
DP   CO          -0.032   0.0       0.0

** Transition from wave guide to horn
DP   B           0.0       #xbw/2   #xbh/2
DP   BZ          0.0       0.0       #xbh/2
DP   BY          0.0       #xbw/2   0.0

** Horn opening
DP   A           #hlen    #hap/2   #hap/2
DP   AZ          #hlen    0.0       #hap/2
DP   AY          #hlen    #hap/2   0.0

** Feed
DP   DS          #feedoff 0.0       0.0
DP   DO          #feedoff 0.0       0.001
DP   DZ          #feedoff 0.0       #xbh/2
DP   DY          #feedoff #xbw/2   0.0

** Create the surfaces in the quadrants y>0 and z>0
** Wave guide end
BP   C  CZ  CO  CY
** Wave guide top
BT   C  CZ  DZ
BQ   C  DZ  BZ  B
** Wave guide walls
BT   C  DY  CY
BQ   C  B  BY  DY
** Horn walls
BQ   B  A  AY  BY
** Horn top
BQ   B  A  AZ  BZ

** Mirroring around the plane z=0 (xy plane). This plane is an
ideal conducting electric wall.
SY  1  0  0  1

** Create half of through feed wire
BL  DS  DY

** Mirror the quarter around the plane y=0 (xz plane). This plane
is an ideal conducting magnetic wall.
SY  1  0  3  0

** Create topside of the feed wire
LA  0

```



```

BL      DO  DZ

** Create the feed segment with the label 1
LA      1
BL      DS  DO

** End of the geometric input
EG      1

** Store matrix elements in .MAT file
PS      0   0   1   0

** The excitation - one frequency point
A1      0       1           1.0       0.0
FR      1   0           10.00e9

** Calculate nearfield
FE      1   1   1   76   0   0.140   0           -0.076   0           0           0.002

** End
EN

```

G.2 E-Plane Sectoral Horn

The FEKO-code for the E-plane sectoral horn is similar to the code for the pyramidal horn. The only code that changes, is the definition of the geometry. This will be given in the program listing.

```

** An E-plane horn for 10 GHz

#MAXLAB=20
#topfrq=10.0e9
#toplam=3E8/#topfrq ** m!!
#segl=#toplam/8
#tril=#toplam/7

** Waveguide dimensions
#xbw=0.02286
#xbh=0.01016

** Horn dimensions
#hap=0.082
#hlen=0.136

```

```

** Feed offset
#feedoff=-0.0256

IP          0.0001    #tril    #segl

** Define the corner points for a quarter of the horn in the
**quadrants y>0 and z>0 with the feed.
LA      2

** Wave guide end
DP      C          -0.032    #xbw/2    #xbh/2
DP      CZ         -0.032    0.0       #xbh/2
DP      CY         -0.032    #xbw/2    0.0
DP      CO         -0.032    0.0       0.0

** Transition from wave guide to horn
DP      B          0.0       #xbw/2    #xbh/2
DP      BZ         0.0       0.0       #xbh/2
DP      BY         0.0       #xbw/2    0.0

** Horn opening
DP      A          #hlen    #xbw/2    #hap/2
DP      AZ         #hlen    0.0       #hap/2
DP      AY         #hlen    #xbw/2    0.0

** Feed
DP      DS          #feedoff 0.0       0.0
DP      DO          #feedoff 0.0       0.001
DP      DZ          #feedoff 0.0       #xbh/2
DP      DY #feedoff #xbw/2 0.0

** Create the surfaces in the quadrants y>0 and z>0
** Wave guide end
BP      C    CZ    CO    CY

** Wave guide top
BT      C    CZ    DZ
BQ      C    DZ    BZ    B

** Wave guide walls
BT      C    DY    CY
BQ      C    B    BY    DY

** Horn walls
BQ      B    A    AY    BY

** Horn top
BQ      B    A    AZ    BZ

```


** Mirroring around the plane $z=0$ (xy plane). This plane is an ideal conducting
**electric wall.

SY 1 0 0 1

** Create half of through feed wire

BL DS DY

** Mirror the quarter around the plane $y=0$ (xz plane). This plane is an ideal
**conducting magnetic wall.

SY 1 0 3 0

** Create topside of the feed wire

LA 0

BL D0 DZ

** Create the feed segment with the label 1

LA 1

BL DS D0

** End of the geometric input

EG 1

Appendix H

Datasheet of the OP500 Phototransistor

Type:	NPN
Part Number:	OP500
Manufacturer Souce Code:	Optek Tech
Device Status:	DISCON
Generic Number:	500
Package Style:	Dome-3.0
Surface Mounted:	NO
Light Current - Minimum:	1.0m
@Irrad-Ee (Cond Light Cur):	1.0m
@VCE (ond of Light Curr):	5.0
Response Time - Maximum:	2.0u
Wavelength - Peak:	875n
I(D) - Absolute Maximum:	100n
@VCE {Cond of I(D)}:	15
V(BR) CEO:	30
I(C) - Absolute Maximum:	
P(D) - Absolute Maximum:	100m
Operating Temp - Minimum:	-40
Operating Temp - Maximum:	100
Reliability:	Commercial
Images Available:	NO
Internal Number:	

Bibliography

- [1] G. Hygate and J. F. Nye, "Measuring microwave fields directly with an optically modulated scatterer," *Measure. Sci. Technol.*, vol. 1, pp. 703–709, 1990.
- [2] R. J. King, *Microwave homodyne systems*. England: Peter Peregrinus LTD., first ed., 1978.
- [3] G. Hygate and J. F. Nye, "Measuring a microwave field close to a conductor," *Measure. Sci. Technol.*, vol. 2, pp. 838–845, 1991.
- [4] J. F. Nye, W. Liang, and G. Hygate, "Mapping a diffraction field close to an obstacle," *IEEE Transactions on Electromagnetic Compatibility*, vol. 37, pp. 288–292, May 1995.
- [5] W. Liang, G. Hygate, J. F. Nye, D. G. Gentle, and R. J. Cook, "A probe for making near-field measurements with minimal disturbance: the optically modulated scatterer," *IEEE Transactions on Antennas and Propagation*, vol. 45, pp. 772–780, May 1997.
- [6] C. C. H. Tang, "Electromagnetic backscattering measurements by a time-separation method," *IRE Transactions on Microwave Theory and Techniques*, pp. 209–213, April 1959.
- [7] A. L. Cullen and J. C. Parr, "A new perturbation method for measuring microwave fields in free space," *Proceedings, IEE*, vol. B102, pp. 836–844, November 1955.
- [8] J. H. Richmond, "A modulated scattering technique for measurement of field distributions," *IRE Transactions—Microwave Theory and Techniques*, vol. MTT-3, pp. 13–15, July 1955.
- [9] K. Iizuka, "How to measure field patterns with photosensitive probes," *Electronics*, pp. 39–43, January 25 1963.

- [10] J. Randa, M. Kanda, and R. D. Orr, "Thermo-optic designs for electromagnetic-field probes for microwaves and millimeter waves," *IEEE Transactions on Electromagnetic Compatibility*, vol. 33, pp. 205–214, August 1991.
- [11] R. F. Harrington, "Field measurements using active scatterers (correspondence)," *Transactions on Microwave Theory and Techniques*, pp. 454–455, September 1963.
- [12] J. V. Hajnal, "Compound modulated scatterer measuring system," *IEE Proceedings*, vol. 134, pp. 350–356, August 1987.
- [13] R. E. Collin, *Foundations for microwave engineering*. New York: McGraw-Hill, Inc., second ed., 1992.
- [14] C. A. Balanis, *Advanced engineering electromagnetics*. New York: John Wiley & Sons, Inc., first ed., 1989.
- [15] D. M. Pozar, *Microwave engineering*. New York: John Wiley & Sons, Inc., second ed., 1998.
- [16] S. Ramo, J. R. Whinnery, and T. van Duzer, *Fields and waves in communication electronics*. New York: John Wiley & Sons, Inc., third ed., 1994.
- [17] R. F. Harrington, *Time-harmonic electromagnetic fields*. New York: McGraw-Hill Book Company, Inc., first ed., 1961.
- [18] R. J. King and Y. H. Yen, "Probing amplitude, phase, and polarization of microwave field distributions in real time," *IEEE Transactions on Microwave Theory and Techniques*, vol. MTT-29, pp. 1225–1231, November 1981.
- [19] G. Strang, *Introduction to linear algebra*. Wellesley MA 02181 USA: Wellesley-Cambridge Press, first ed., 1993.
- [20] F. G. Stremler, *Introduction to communication systems*. Massachusetts: Addison-Wesley Publishing Company, Inc., third ed., 1990.
- [21] R. E. Ziemer and W. H. Tranter, *Principles of communications*. New York: John Wiley & Sons, Inc., fourth ed., 1995.
- [22] P. Z. Peebles, *Probability, random variables, and random signal principles*. New York: McGraw-Hill, Inc., third ed., 1993.

- [23] R. E. Collin, *Antennas and radiowave propagation*. New York: McGraw-Hill Book Company, first ed., 1985.
- [24] J. G. Proakis and D. G. Manolakis, *Digital signal processing principles, algorithms and applications*. USA: Prentice-Hall International, Inc., third ed., 1996.
- [25] J. W. B. Davenport and W. L. Root, *An introduction to the theory of random signals and noise*. New York: IEEE Press, 1987.
- [26] J. H. Cloete, "Averaging." Personal Communication, October 2000.
- [27] Burr-Brown, "Single-ended analog input 20-bit stereo analog-to-digital converter," pcm1800, Burr-Brown Corporation, PO Box 11400, Tucson, AZ 85734, August 1997.
- [28] W. Steyn, "A room temperature X-band receiver front end optimised for introduction of high temperature superconductor technology." Master's Thesis, December 1998.
- [29] D. A. McNamara, C. W. I. Pistorius, and J. A. G. Malherbe, *Introduction to the uniform geometrical theory of diffraction*. Boston, London: Artech House, first ed., 1990.
- [30] R. G. Kouyoumjian and P. H. Pathak, "A uniform geometrical theory of diffraction for an edge in a perfectly conducting surface," *Proceedings IEEE*, vol. 62, pp. 1448–1461, November 1974.
- [31] E. V. Jull, *Aperture antennas and diffraction theory*, vol. 10 of *Electromagnetic wave series*. London: Peter Peregrinus LTD., first ed., 1981.
- [32] D. G. Zill and M. R. Cullen, *Advanced engineering mathematics*. Boston: PWS Publishing Company, first ed., 1992.
- [33] W. L. Stutzman and G. A. Thiele, *Antenna theory and design*. New York: John Wiley & Sons, Inc., second ed., 1998.
- [34] J. D. Kraus, *Antennas*. New York: McGraw-Hill Book Company, Inc., second ed., 1988.
- [35] K. D. Palmer, "Antenna theory 813." Course Work for Masters in Engineering: University of Stellenbosch, 1999.
- [36] E. Burger, "Marconi horn FEKO model." Personal Communication, June 2000.